AD-780 037

MECHANICAL PROPERTIES OF TWO HIGHLY POROUS GEOLOGIC MATERIALS

F. H. Shipman, et al

Terra Tek, Incorporated

Prepared for:

Army Materials and Mechanics Research Center

April 1974

REPORT DOCUMENTATION PAGE		READ INSTRUCTIONS BEFORE COMPLETING FORM
1. REPORT NUMBER AMMRC CTR 74-25	2. GOVT ACCESSION NO.	3. RECIPIENT'S CATALOG NUMBER AD 780037
4. TITLE (and Subtitle) Mechanical Properties of Two Highly Porous Geologic Materials		5. TYPE OF REPORT & PERIOD COVERED Final - April 1972 to April 1973
		6. PERFORMING ORG. REPORT NUMBER TR 73-45
7. AUTHOR(s) F. H. Shipman J. N. Johnson S. J. Green		8. CONTRACT OR GRANT NUMBER(s) DAAG46-72-C-0169
9. PERFORMING ORGANIZATION NAME AND ADDRESS Terra Tek, Inc. 420 Wakara Way Salt Lake City, Utah 84108		10. PROGRAM ELEMENT, PROJECT, TASK AREA & WORK UNIT NUMBERS D/A Project: 1W162113A661 AMCMS Code: 612113.11.D7000 Agency Accession: -
11. CONTROLLING OFFICE NAME AND ADDRESS Army Materials and Mechanics Research Center Watertown, Massachusetts 02172		12. REPORT DATE April 1974
		13. NUMBER OF PAGES 65
14. MONITORING AGENCY NAME & ADDRESS(if different from Controlling Office)		15. SECURITY CLASS. (of this report)
		15a. DECLASSIFICATION/DOWNGRADING SCHEDULE

16. DISTRIBUTION STATEMENT (of this Report)

Approved for public release; distribution unlimited.

17. DISTRIBUTION STATEMENT (of the abstract entered in Block 20, if different from Report)

18. SUPPLEMENTARY NOTES

19. KEY WORDS (Continue on reverse side if necessary and identify by block number)

Rock properties	Porous materials
Rock mechanics	Triaxial stresses
Hydrostatic strength	Fracture

20. ABSTRACT (Continue on reverse side if necessary and identify by block number)

Hydrostatic pressure, compression under different confining pressures, proportional loading and uniaxial-strain tests were conducted on a dry tuff from the Nevada Test Site and dry Kayenta sandstone from the Mixed Company Site near Grand Junction, Colorado. Both rocks exhibit behavior which is characteristic of very porous geological materials; namely, increasing shear strength as a function of confining pressure, large volume compaction followed by volume dilatancy under selected loadings with enhanced compaction,

DD FORM 1473 EDITION OF 1 NOV 65 IS OBSOLETE

over some pressure ranges, in the presence of shear deformation. Both materials also exhibit strain work-hardening. A "cap model" is applied to represent the mechanical behavior of these two materials. This model accounts for all of the aforementioned characteristics of both the tuff and the sandstone, and provides a means to represent the path dependence of their mechanical properties.

ia

FOREWORD

This report describes the work performed by Terra Tek, Inc. for the Army Materials and Mechanics Research Center (AMMRC) under Contract No. DAAG46-72-C-0169. The project was accomplished as part of the U.S. Army Reduction-of-Vulnerability of ABM Systems Program. Program Manager at AMMRC was Mr. J. F. Dignam. The Contracting Officer Representative at AMMRC was Dr. S. C. Chou.

i

TABLE OF CONTENTS

LIST OF ILLUSTRATIONS

I. INTRODUCTION

A shallow-buried structure, such as an ABM silo, may be made relatively safe from nuclear and thermal radiation and from the direct effects of air-blast. The primary vulnerability, therefore, is associated with the motion of the surrounding earth. In addition to the intense direct shock in the ground that is responsible for the crater formation from a surface burst, ground motions are induced by the passage of an air blast wave along the surface. For most surface or shallow buried structures, this air-induced ground shock is of great significance since it is extended to large distances, while the direct ground shock is more rapidly attenuated in passing through the intervening earth mass.

In the past, direct ground shock was calculated using hydrodynamic models while air-induced ground shock effects were approximated by means of linear elastic models. Experimental data has shown that these models do not represent geologic materials well, and hence more realistic models are required. To calculate both the intense direct ground shock and the air-induced ground shock requires a description of the material behavior in the stress range extending from Megabar stresses, which occur near ground zero, down to very low stresses, which occur at large distances from ground zero. It is probably the stress region between the very high stresses, which may be reasonably well represented by a hydrodynamic model, and the extremely low stresses which may reasonably well be represented by linear elasticity, that require the most complicated constitutive model. In particular, the stress region from the linear elastic region to ten's of kilobars requires

1

the most attention. This is the stress region covered by the work here.

Stress-strain data for two geological materials have been obtained from a variety of load-path tests. The two geologic materials were selected to represent two extremes in very porous geologic materials; one with relatively "weak cementing of grains" and the other with relatively "strong cementing of grains." The tests serve two major purposes: (i) to give the general characteristic stress-strain behavior in order to build mathematical models that qualitatively fit the behavior at the appropriate stress levels, and (ii) to provide quantitative data from which the required material constants in the mathematical models can be determined.

The observed data are fit with a "cap model." This elastic-plastic model accounts for the general features and fits the hydrostatic pressure and compression response under different confining pressures very well. Some shortcomings of the "cap model" as applied here are discussed and some in-situ, real rock mass effects are mentioned.

II. EXPERIMENTAL RESULTS

Experimental Techniques

Loading Presses

Laboratory tests were conducted on small solid cylindrical samples using servocontrolled testing machines.[1] The samples were subjected to fluid confining pressure and to axial compression simultaneously. By programming the application of the load and the application of the fluid pressure independently, a variety of load-path tests were conducted.[2] Figure 1a shows the servocontrolled loading presses used for tests here.

Sample Size

Test specimens were made by diamond coring and finish grinding samples to final dimensions of 1.9 cm (.75 inch) diameter by 3.8 cm (1.50 inch) long. The specimens were covered with .25 mm thick urethane sheet and metal end caps were epoxied to the specimen ends. The urethane sheet prevented fluid intrusion, but carried an insignificant load.[2] More details of test specimen preparation are contained in Appendix B.

Measurement of Stresses and Strains

All stresses and strains were measured inside the pressure vessel,[1,2] and therefore corrections for seal-friction, alignment, pressure and temperature effects were either not needed or were measured directly. Pressure was measured with a manganin pressure coil; load was measured using a load-cell adjacent (axially in-line with) to the test specimen. Axial and transverse strains were measured using cantilevered displacement measuring devices, precalibrated
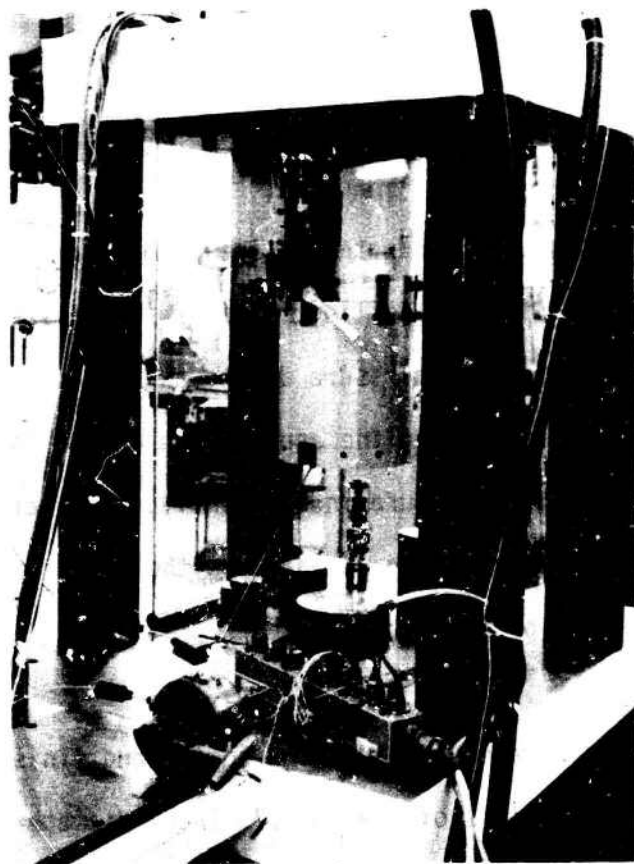
3

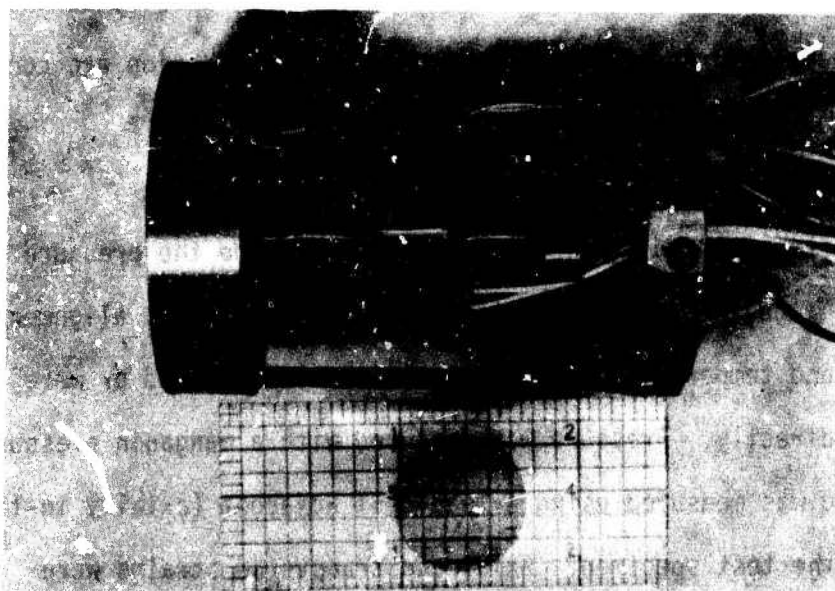Figure 1a. 10 kbar testing machine.

Figure 1b. Test specimen with cantilever.

Figure 1. Test Apparatus.

4

inside the pressure vessel. The axial-cantilever displacement sensor
provided a measure of average specimen shortening, while the trans-
verse-cantilever sensor provided measurement of average diameter
change at two diameters. Figure 1b shows the test specimen with the
axial and transverse strain sensors attached.

Accuracy of Measurements

The pressure measurement is accurate to ±10 bars and load to ±10
bars. The cantilever displacement sensors give cantilever displacements
accurate to $\pm5 \times 10^{-4}$ mm. Average specimen strains are measured accur-
ate to better than 500 microstrains (5×10^{-4} strain). Uncertainty
in measuring strains is due to the specimen jacket materials and the
specimen-jacket interface. Repeatability of several tests is shown
by scatter bars on the figures.

All tests were conducted at room temperature; the loading was
such as to give strain rates of about 10^{-4}/second. Details of the
techniques are contained in Appendix A. Throughout this work the
volume strain is calculated according to the small strain approximation,
i.e., $\Delta V/V_0 = \epsilon_1 + 2\epsilon_3$, where ϵ_1 and ϵ_3 are the axial and transverse
strains, respectively. The error involved in this approximation is
shown in Appendix A to be less than the scatter of the individual
test data. This approximation is also commensurate with mathematical
models for porous rock behavior, such as the one given in Section IV.

Material Description

The two materials tested were an ash-fall tuff from the Nevada
Test Site[3] and a competent sandstone from the Mixed Company high-
energy explosive site near Grand Junction, Colorado.[4] Physical

properties are given below; more detailed descriptions of the rocks
are included in Appendix B. All tests were conducted on "dry" samples.
The effect of water content on the mechanical properties of tuff and
sandstone is beyond the scope of this report and remains to be fully
investigated.

TABLE 1. PHYSICAL PROPERTIES OF ROCKS TESTED

	Dry Density gm/cm^3	Grain Density gm/cm^3	Total Porosity % of Volume	Grain Size	Pore Size
Tuff	1.7	2.46	31	< 1mm (fragments to 5mm)	10^{-7}mm to > 1 mm
Sandstone	2.0	2.66	25	0.2 - 0.3 mm	0.1 mm

Experimental Results on Tuff

Loading Paths

A number of different loading paths were selected, including:
(1) hydrostatic pressure, (2) compression under different constant
confining pressures from zero to 8 kbars (triaxial-stress), (3)
uniaxial-strain and (4) proportional-stress. During these tests the
stress state is given below in Table 2, where the 1 direction refers
to the axis of the cylindrical specimen and 2 and 3 are transverse
orthogonal directions. Compressive loading and shortening strains
are taken as positive. All stress-strain values are engineering
stress-strain, without correcting for geometry changes.

6

TABLE 2. STRESS STATES FOR VARIOUS LOADING PATHS

	Stress-State
Hydrostatic	$\sigma_1 = \sigma_2 = \sigma_3$
Triaxial Stress	$\sigma_1 > \sigma_2 = \sigma_3$
Uniaxial Strain	$\begin{pmatrix} \sigma_1 > \sigma_2 = \sigma_3 \\ \epsilon_2 = \epsilon_3 = 0 \end{pmatrix}$
Proportional Stress	$\begin{pmatrix} \sigma_1 > \sigma_2 = \sigma_3 \\ \sigma_1/\sigma_3 = \text{const.} \end{pmatrix}$

The loading paths are shown in Figure 2, where the load, i.e., stress difference $(\sigma_1 - \sigma_3)$, has been plotted versus the mean normal stress for each of the different kinds of tests. Each line represents the average of three to five tests, with the loading preceding
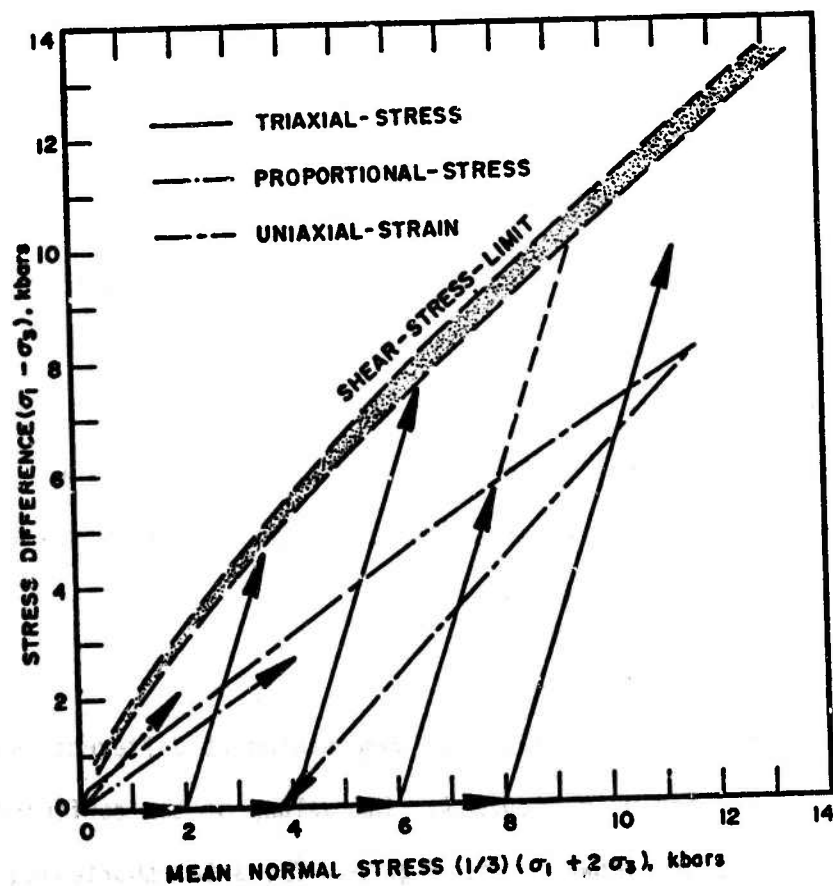

Figure 2. Loading paths for dry NTS ash-fall tuff.

to the end of the line as shown. Unloading follows identically the loading paths except for the uniaxial-strain tests. The hydrostatic-pressure tests lie along the mean normal stress axis, while triaxial-stress, uniaxial-strain and proportional-stress tests are shown with different symbols. The "shear-stress limit" curve is an estimate of what is conventionally called the "failure envelope." This limit-curve constitutes a maximum shear-stress (load here) that can be reached for any path of loading;[5] i.e., stress states beyond this curve are not possible. The locus of this curve is determined by the asymptotic limit to the stress difference $\sigma_1 - \sigma_3$ as a function of the axial and transverse strains in a triaxial compression test.

Hydrostatic Tests

The hydrostat for this tuff is snown in Figure 3, where the volume strain, $\Delta V/V_0$, is obtained as the measured axial strain plus the two transverse strains. Axial and transverse strains were measured and the results suggest isotropic response. Even though large volume strains occur, approximately ten percent porosity still exists at 8 kbars pressure. Apparently much higher pressure is required to completely compact all porosity. Several unloadings and reloadings are shown. Considerable recovery occurs as is noted by the bend-back of the hydrostat when unloading from 8 kbars, for example.

Triaxial-Stress Tests

The stress-strain curves for compression at different confining pressures are shown in Figure 4. The values of the confining pressure, σ_3, are shown in the figure. The axial shortening strain and the transverse extension strain during the compressive loading
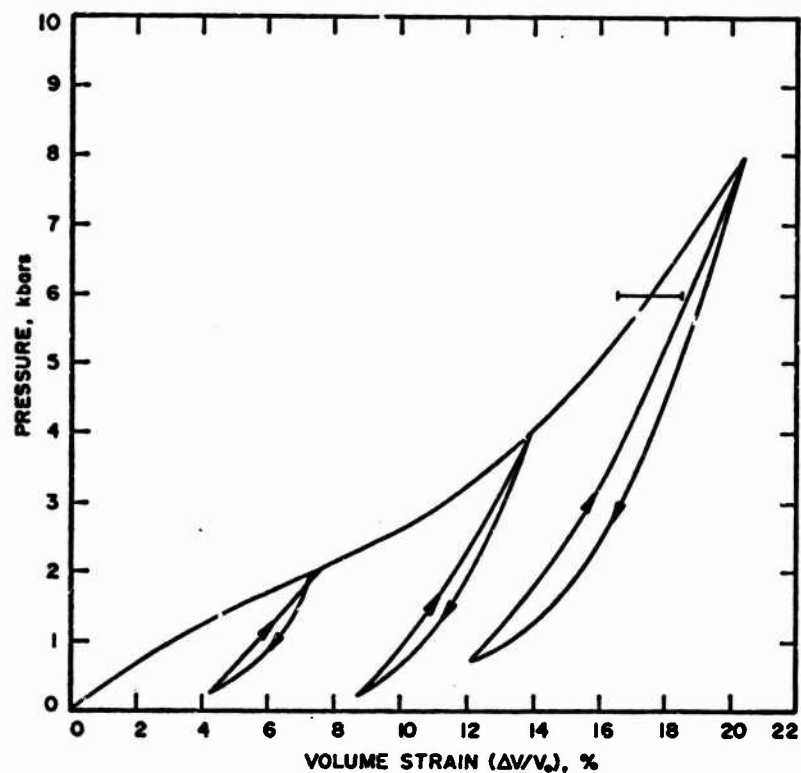
8

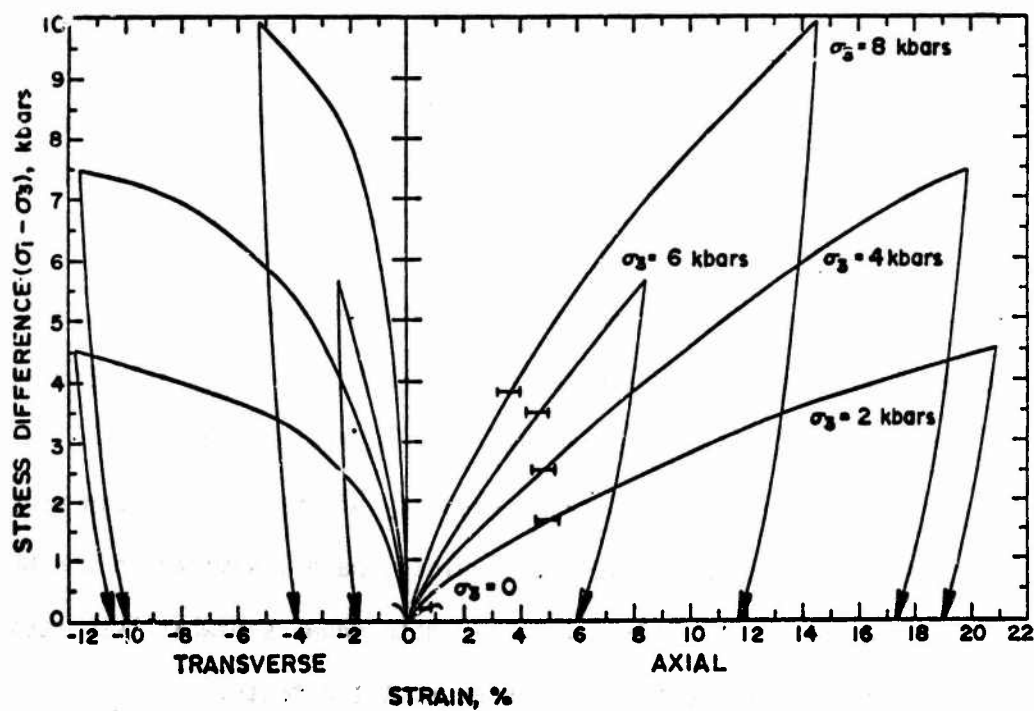Figure 3. Hydrostat for dry NTS ash-fall tuff.

Figure 4. Triaxial compression tests for dry NTS ash-fall tuff.

9

are shown. From this figure, shear strain and volume strain can be obtained (and are shown later), as well as the apparent elastic constants, Young's modulus and Poisson ratio. A large increase in Young's modulus is shown with increasing confining pressure. A transition from brittle behavior, for the unconfined compression test, to ductile behavior for all the confined tests, occurs when brittle refers to an abrupt load drop after some maximum stress and ductile refers to the ability to undergo large crushup strains without a load drop. Work-hardening, or strain strengthening, occurs to very large strains for the confined tests. Unloading occurs along a much steeper modulus than loading.

Uniaxial-Strain and Proportional-Stress Tests

The stress-strain curves for uniaxial-strain and two different proportional stress paths* $\sigma_1/\sigma_3 = 1.88$ and $\sigma_1/\sigma_3 = 2.81$, are shown in Figure 5. Here the axial and transverse strains are the "total" strains starting from zero stress, and from these the shear and volume strains can again be obtained.

The $\sigma_1/\sigma_3 = 1.88$ proportional-stress and the uniaxial-strain tests follow relatively similar paths, while the $\sigma_1/\sigma_3 = 2.81$ proportional-stress tests show much less work hardening and greater transverse strain. Considerable recovery of the axial strain occurs for the proportional-stress load (unload) paths, similar to the hydrostat, Figure 3. The uniaxial-strain path shows somewhat less recovery on unloading than the triaxial or hydrostatic tests.

---

* These two stress paths are chosen by drawing the approximate location of the desired stress path on graph paper and then accurately measuring the slope followed after the test is completed. There is no special significance to the particular values of σ_1/σ_3 used here.
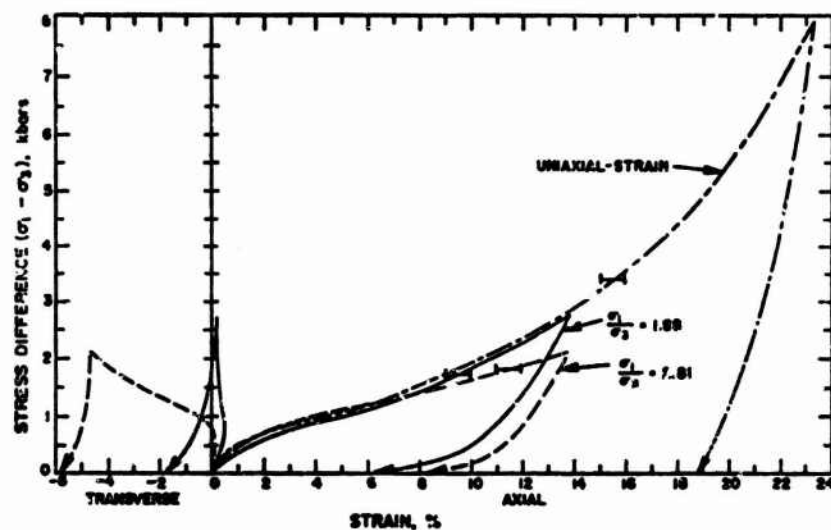
Figure 5.   Uniaxial-strain and proportional-stress
tests on dry NTS ash-fall tuff.

Experimental Results on Sandstone

Loading Paths

The different load paths selected were similar to those for the
tuff. Figure 6 shows the load versus mean normal stress for the
different paths; each path represents the average of three to five tests.
Again the hydrostatic pressure loading lies along the mean normal stress
axis, while other paths are shown with different symbols. The sandstone
shows a shear-stress limit relatively similar to the tuff, up to mean
normal stress of about 4 kbars. For higher mean normal stresses the
shear strength appears to be plateauing, increasing only slightly with
mean normal stress. The uniaxial-strain path shown in Figure 6 for sand-
stone differs significantly from the nearly linear response shown in
Figure 2 for the tuff.

11
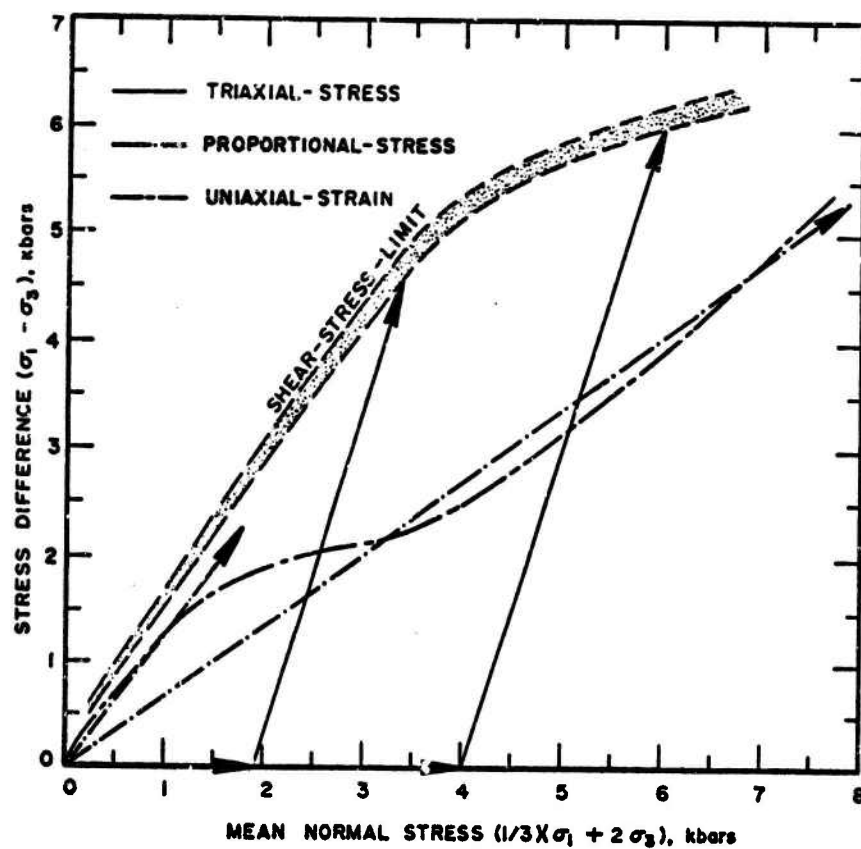
Figure 6. Loading paths for sandstone.

Hydrostatic Tests

The hydrostat for the dry sandstone is shown in Figure 7. As for the tuff, the axial and transverse strains were approximately equal, suggesting isotropic response. The sandstone, unlike the tuff, shows a "foot," or elastic compaction, up to about .3 to .4 kbars pressure. This is believed due to closing of micro-cracks which exist in the sandstone. Large permanent compaction occurs for pressures above about 4 kbars. However, the volume compaction of about 15% at 8 kbars pressure indicates that not all the initial 25% void space has been compacted, even at this high pressure. The competent intact sandstone specimen becomes "crushed" and broken for pressures above about 4 kbars and appears to be loose "sand" after unloading.
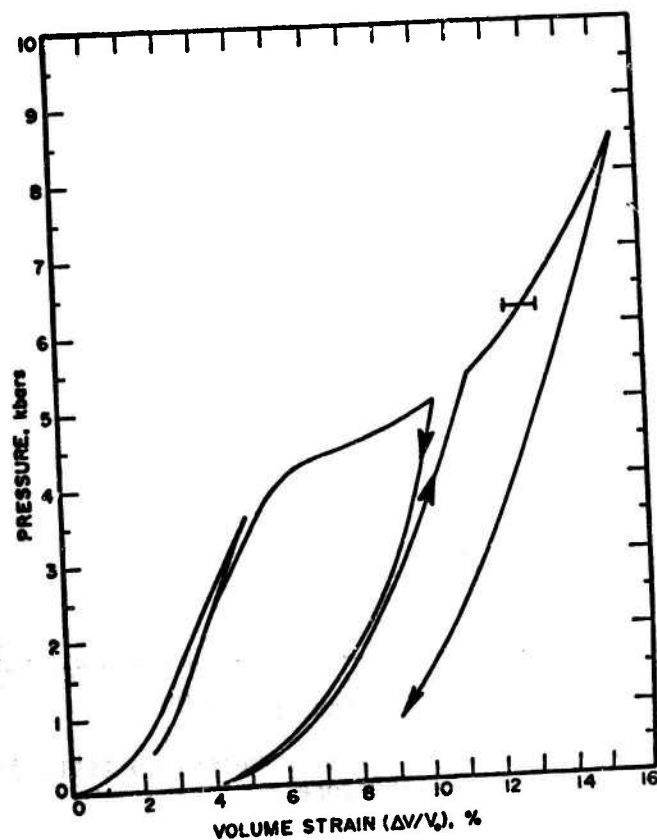
Figure 7. Hydrostat for dry sandstone.

13

Triaxial-Stress Tests

The stress-strain curves for compression at different confining pressures are shown in Figure 8, where axial shortening strain and transverse extension strain are plotted versus the compressive load. The confining pressures are shown on each curve as σ_3. Increase in the Young's modulus is shown with increasing confining pressure and a transition from brittle behavior for the unconfined test to ductile behavior for all the confined tests occurs. Work hardening, or strain strengthening, is shown (for the confined tests) to very large shortening strains. Unloading occurs along a much steeper modulus than loading.
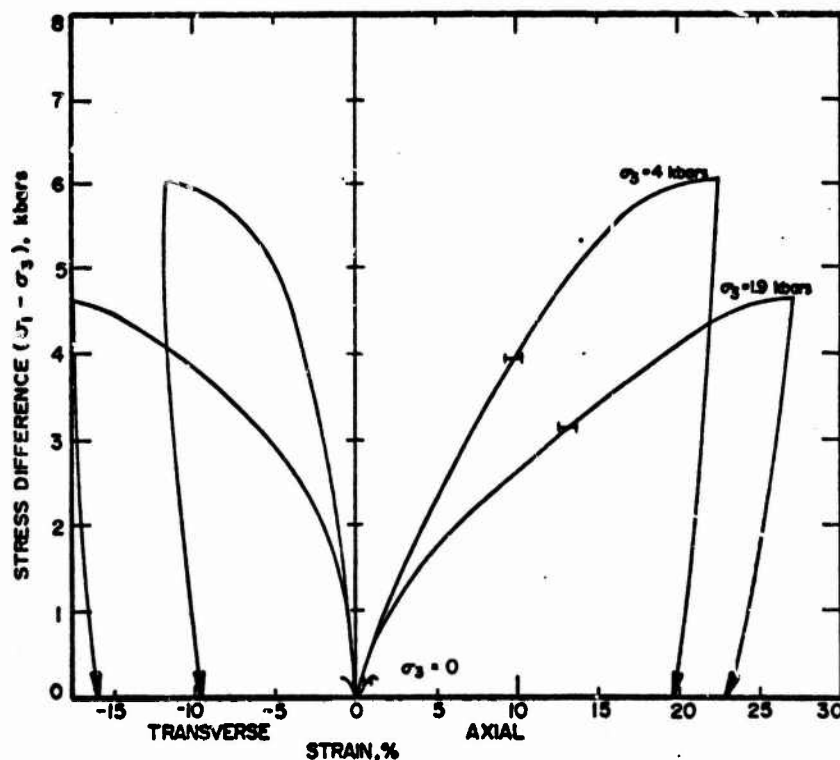
Figure 8. Triaxial compression tests for dry sandstone.

14

Uniaxial-Strain and Proportional-Stress Tests

The stress-strain curves for uniaxial-strain and proportional-stress, $\sigma_1/\sigma_3 = 1.88$ and $\sigma_1/\sigma_3 = 3.18$, loadings are shown in Figure 9. Axial and transverse strains are "total" strains starting from zero stress. From these curves, shear-strain and volume-strain can be determined and are presented later.

Just as for the tuff, the $\sigma_1/\sigma_3 = 1.88$ proportional-stress test and the uniaxial-strain tests follow relatively similar paths. The higher stress ratio proportional-stress test shows less (no) work hardening and larger transverse strain.

Figure 9. Uniaxial-strain and proportional-stress tests on dry sandstone.

15

III. GENERAL FEATURES

Hydrostatic Compression

Hydrostatic compaction at low pressure, up to hundreds of bars for the dry tuff and about 4 kbars for the dry sandstone, will give elastic, but generally non-linear, response with no or little measurable permanent set.[6] The initial bulk modulus in this approximately elastic region would agree with that calculated from ultrasonic velocity measurements of shear and longitudinal velocities, except that (i) strain-rate effect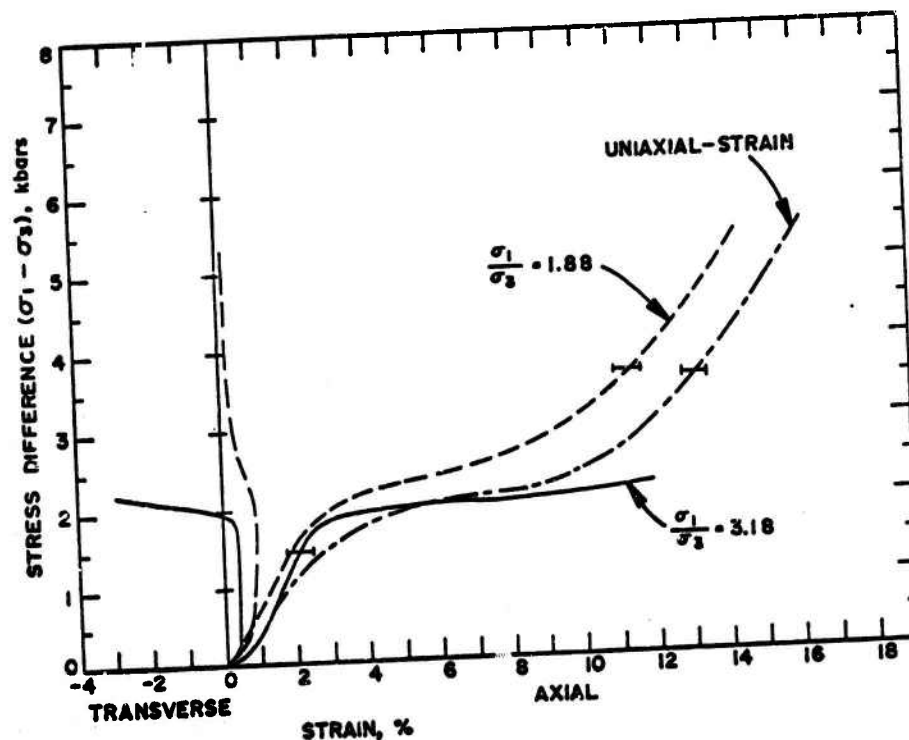s are neglected and (ii) ultrasonic pulses are of a micro-strain magnitude whereas even for pressures of bars the strains are orders-of-magnitude greater and hence, may result in different deformation mechanisms. The calculated elastic constants from measurement of shear and longitudinal velocities[7] (of dry sandstone and dry tuff[6] with similar density and porosity) and the average initial bulk modulus (from Figures 3 and 7) are shown in Table 3.

TABLE 3. INITIAL ELASTIC CONSTANTS

	Shear Velocity mm/µsec (1 MHz)	Longitudinal Velocity mm/µsec (1 MHz)	Calculated From Ultrasonic Measurements					Initial Bulk Modulus From Hydrostat K, kbars
			Constrained Modulus B, kbars	Bulk Modulus K, kbars	Young's Modulus Y, kbars	Poisson Ratio γ	Shear Modulus G, kbars	
Dry NTS Tuff	1.52	2.63	117	64.8	97	.25	39	36
Dry Sandstone	1.53	2.20	97	34.6	97	.03	47	"foot" 14 "linear" 118

The average slope of the hydrostat in the approximately elastic region does not agree with that obtained from ultrasonic velocity measurements.[6] This can be seen in Figure 10, where the slope obtained from ultrasonic measurements, labeled ultrasonic K, has

been added to the hydrostat. For the tuff, an average slope for the approximately elastic region has been drawn, labeled hydrostatic K. For the sandstone, an average slope up to .2 to .3 kbars pressure would be less than the ultrasonic K, but an average slope from .5 to 3.5 kbars pressure would be greater, as shown on Figure 10b.
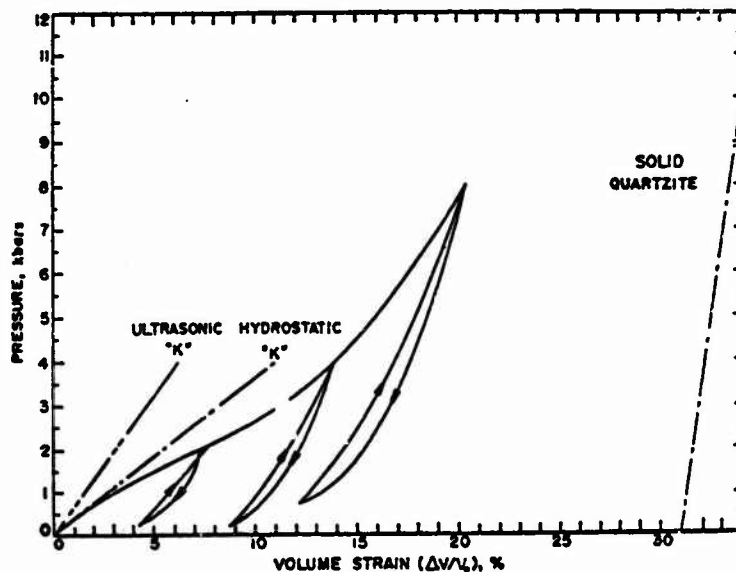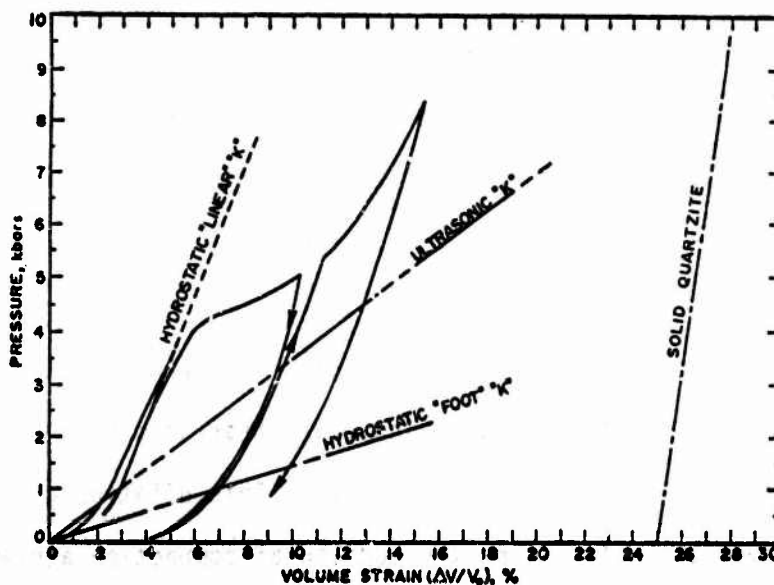

Figure 10a. Dry NTS tuff.

Figure 10b. Dry sandstone.

Figure 10. Hydrostatic response.

17

As the hydrostatic pressure is increased--beyong the approximately elastic region--massive crushup of the rock occurs. The rock has "yielded" under bulk hydrostatic pressure. Crushup continues until the porosity has been eliminated. However, the pressure volume-change curve steepens considerably well before all porosity is removed. It is clear from Figure 10 that high mean normal stresses are required to eliminate the porosity; i.e., for the hydrostat to approach closely the "solid" curve (taken approximately as quartzite) offset by a volume strain equal to the initial porosity.

Hydrostatic Compression Plus Shear Stress

The addition of shear stress to a hydrostatic compression in highly porous rocks has the effect of increasing the volume strain over some stress range.[2,8-10] That is, stress can help to collapse the structure, and more porosity is removed for a given mean normal stress. This is shown clearly in Figure 11 where all load paths containing shear stress lie on the compacted side of the hydrostat for some stress region. In this figure the curves marked with σ_3 refer to the triaxial-stress tests and the curve marked σ_1/σ_3 to the proportional-stress tests.

Dilation (which occurs under selected load paths[11]) tends to exceed compaction as the specimen nears the peak shear-stress it will support, in the constant confining pressure tests. This dilation gives a volume increase more than offsetting the additional compaction achieved under compression at constant confining pressure. Surprisingly, dilation occurs when all three stresses are compressive, even for materials that contain large porosity.

18
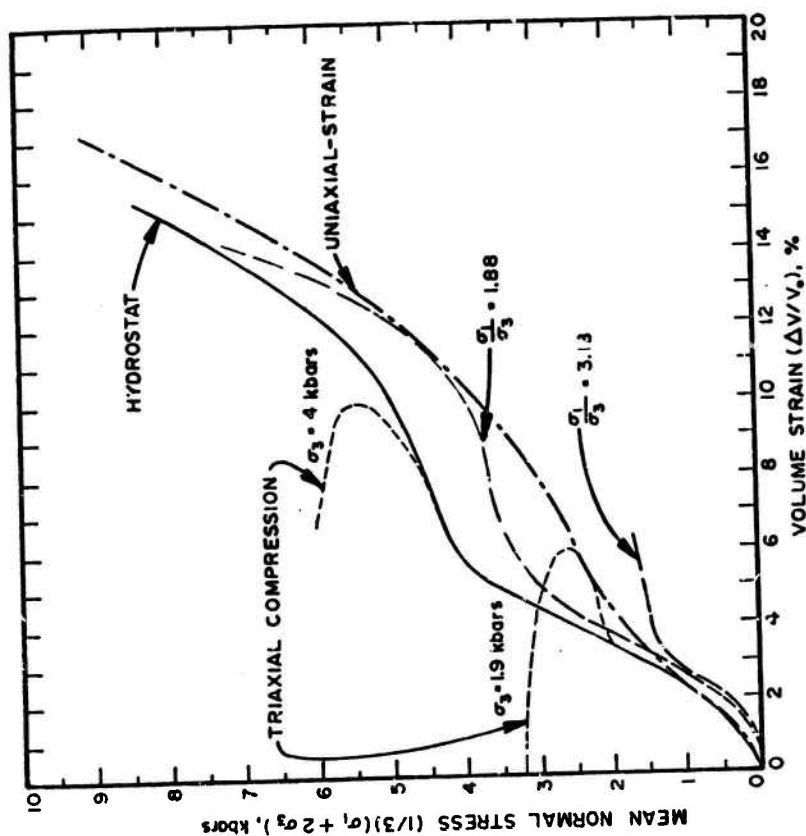
Figure 11b. Dry sandstone.
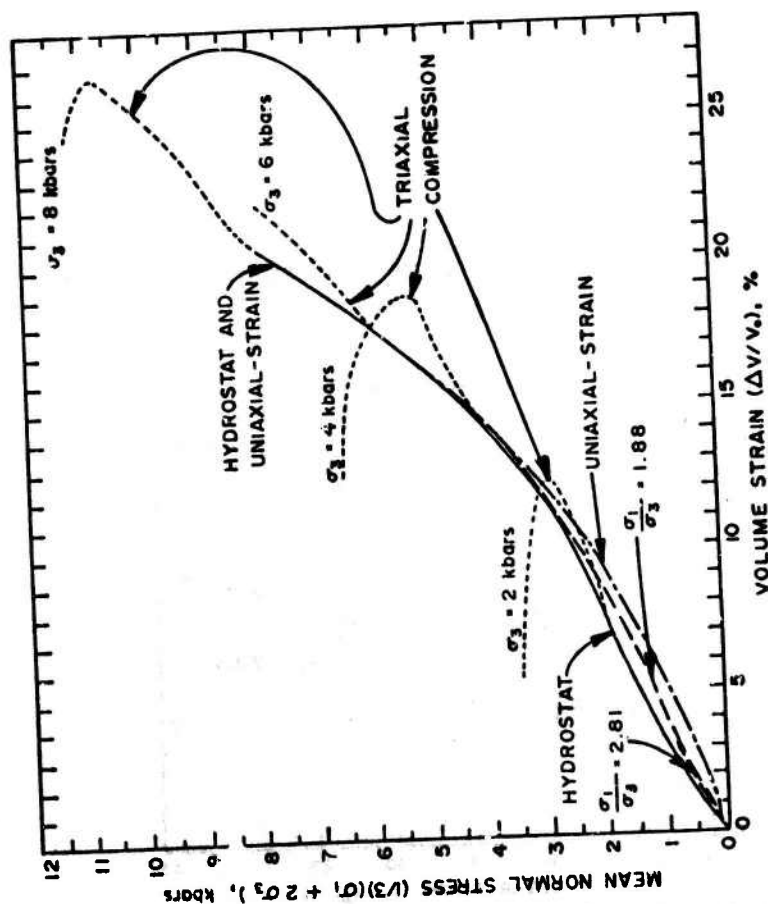
Figure 11a. Dry NTS tuff.

Figure 11. The effect of hydrostatic compression plus shear stress.

19

Shear Strains for Various Loading Paths

The shear-stress/shear-strain curves for various loading paths
are shown in Figure 12. An increase in apparent shear modulus and
shear strength with pressure is seen.[12,13] Work hardening occurs
over a large strain range; however, it should be noted that if the
stress-strain curves, Figures 4 and 8, were replotted in terms of
true-stress and natural-strain, the apparent increase in shear
strength at high shear strains would be much less.
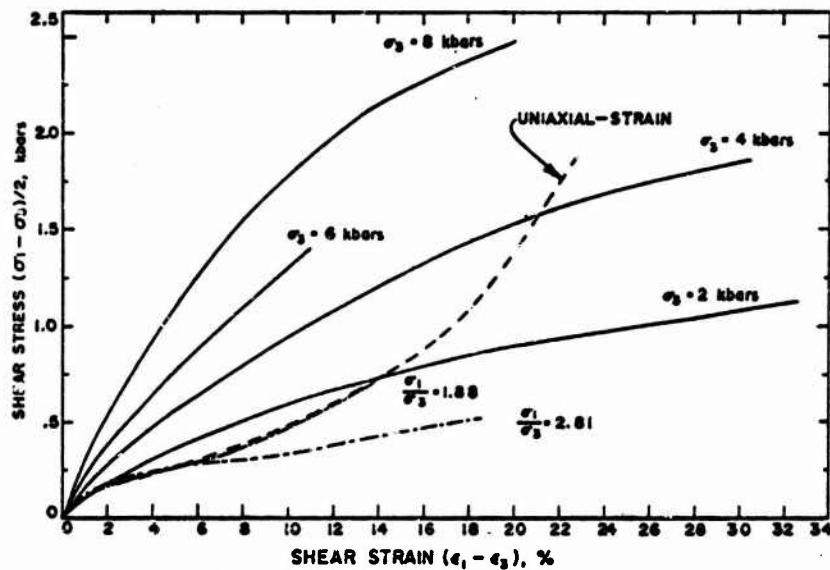
Figure 12a.   Dry NTS tuff.
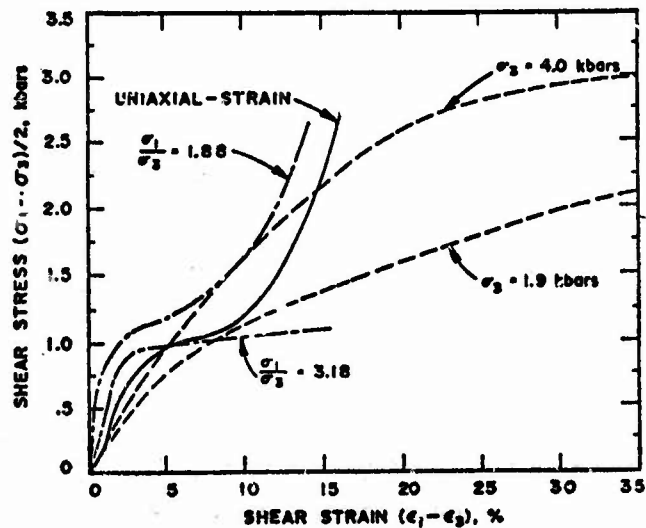
Figure 12b.   Dry sandstone.

Figure 12.   Shear strains for various loading paths.

20

Yield and Fracture

Generally, rocks tend to behave in a brittle manner up to some confining pressure and then undergo a transition to a ductile type crushup with further increase in mean normal stress.[14] Both brittle and ductile need to be qualified, though. Brittle behavior means a relatively abrupt decrease in load-carrying ability, and results in a fractured sample. The stress-strain curve generally does not show an instantaneous drop of stress, but instead may show a decrease in load-carrying ability with increasing strain.[15] Ductile behavior refers to the ability to undergo appreciable strain without any abrupt drop in load, analogous to plastic flow, but generally not "plasticity" in the sense of dislocation motion. After ductile flow a sample may be highly fractured, as for the case of the sandstone here, or it may be intact with relatively little visual evidence of crushup, as for the case of the tuff.

The brittle fracture and ductile crushup may be indicated in stress-space as shown in Figure 13. Many tests are required to define even approximate details of the initial yield surface (whether it be brittle failure or ductile failure) and its subsequent displacement due to work-hardening. Some estimates can be made, however, from Figure 13. The initial yield under hydrostatic compression for this tuff has been defined by point A, point B defines the yield point under unconfined compression, and point C, the yield under uniaxial-strain loading. These three points approximate the initial yield surface; however, this is at best only as good as the ability to distinquish the yield during each of these tests.
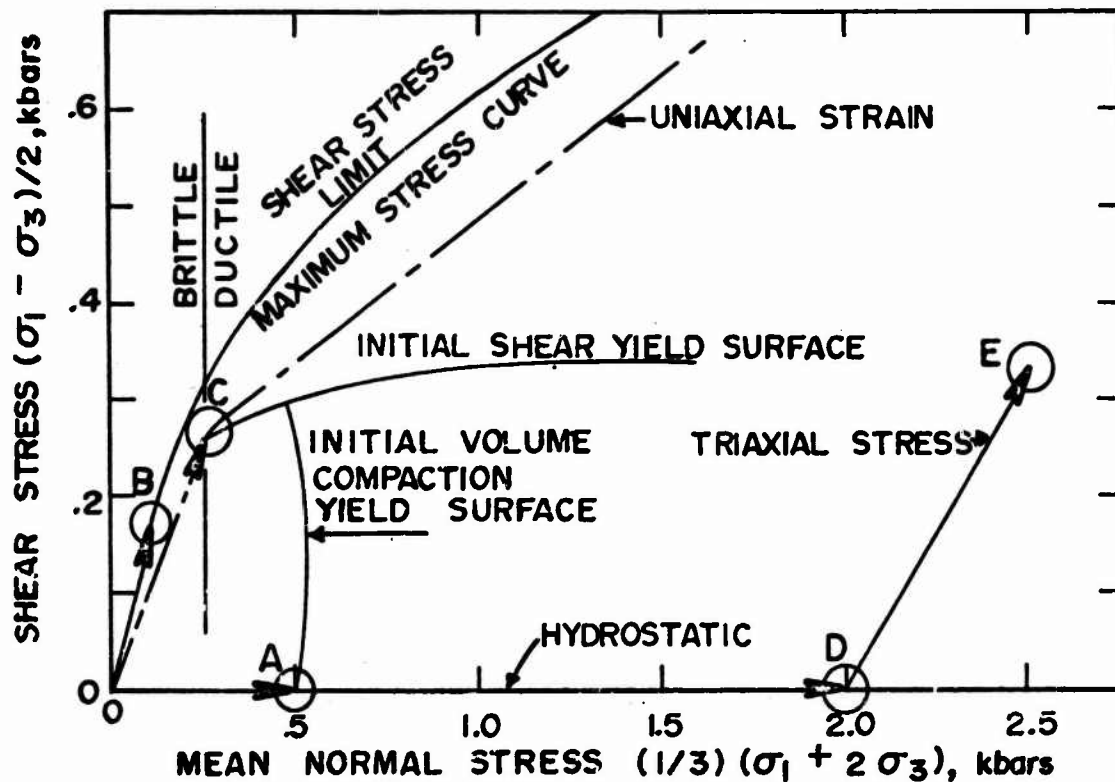
Figure 13. Brittle fracture and ductile crushup for tuff.

Less information exists regarding subsequent yield surfaces.
The data show that if hydrostatic loading occurs to point D, unloading
and reloading produce (at least approximately) elastic behavior
until point D is reached again (see Figures 3 and 7). Hence the
yield surface has been moved from point A to point D.

Loading along a path to point E (Figure 13) is well into the
inelastic region. Unloading and reloading a "small" load increment
generally produces elastic behavior until point E has been reached
again during reloading.[16] Unloading and reloading a "large" load in-
crement (say all the shear load) does not necessarily produce elastic
behavior.[16] Hence, the subsequent yield surface after reloading is
not well defined, and many more tests than those conducted here are
required.

22

Path Dependence

Tests have shown a general path independence of the brittle
failure shear strains of low-porosity rocks,[5] and some evidence exists
to suggest shear stress limit in the ductile region (Figures 2 and
6) is also relatively path independent.[5,16] However, this path inde-
pendence does not apply if plastic deformation occurs on one side of
the brittle-ductile transition and the maximum stress is reached on
the other side.[16]

The path independence (or dependence) of strains has not been
so well defined, however. Some data suggest only a weak path de-
pendence for loading just in a range where rocks fail brittlely.[17]
This is the consequence of the small inelastic deformation which
occurs prior to brittle failure. The data here, in the ductile ranges,
suggest a relatively strong path dependence of strains due to large
inelastic deformation. This is shown when Figure 14 is combined with
Figure 2. For example, the 4 kbar constant confining pressure test
crosses the uniaxial-strain loading path at a stress difference of 4
kbars (see Figure 2). At this point $\sigma_1 = 8$ kbars, $\sigma_2 = \sigma_3 = 4$ kbars
for both tests. From Figure 14 it is apparent that the axial strains
are not the same for both tests at $\sigma_1 = 8$ kbars, nor are the shear or
volume strains. The same reasoning can be made by selecting similar
strain states from Figure 14 and noting the different stress states in
Figures 14 and 2 (using an interpolation of stresses). Similar behavior
was observed for the sandstone.

23
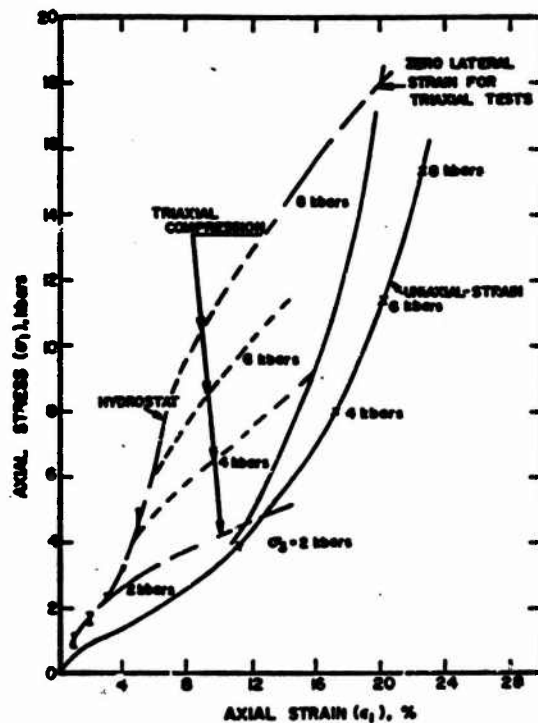
Figure 14. Path dependence for tuff.

Dynamic Effects

Low-to-intermediate strain-rate data and plane shock-wave data exist for tuff.[18,19] These data show a 7 percent increase in failure stress per decade increase in strain rate, but are for material with an average density of 1.45 gm/cm^3: comparison with the static response of 1.7 gm/cm^3 samples would therefore have little meaning. There do exist, however, shock-wave data on dry Mixed Company sandstone from the same location as the material used in the static tests.[18] These data are from dynamic plate-impact experiments which produce conditions of uniaxial strain. The dynamic uniaxial-strain response from two plate-impact experiments is compared with the static data in Figure 15. It can be seen that there is

considerable variation in the shock-wave data: therefore, firm con-
clusions regarding the magnitude of dynamic effects are difficult
to make.
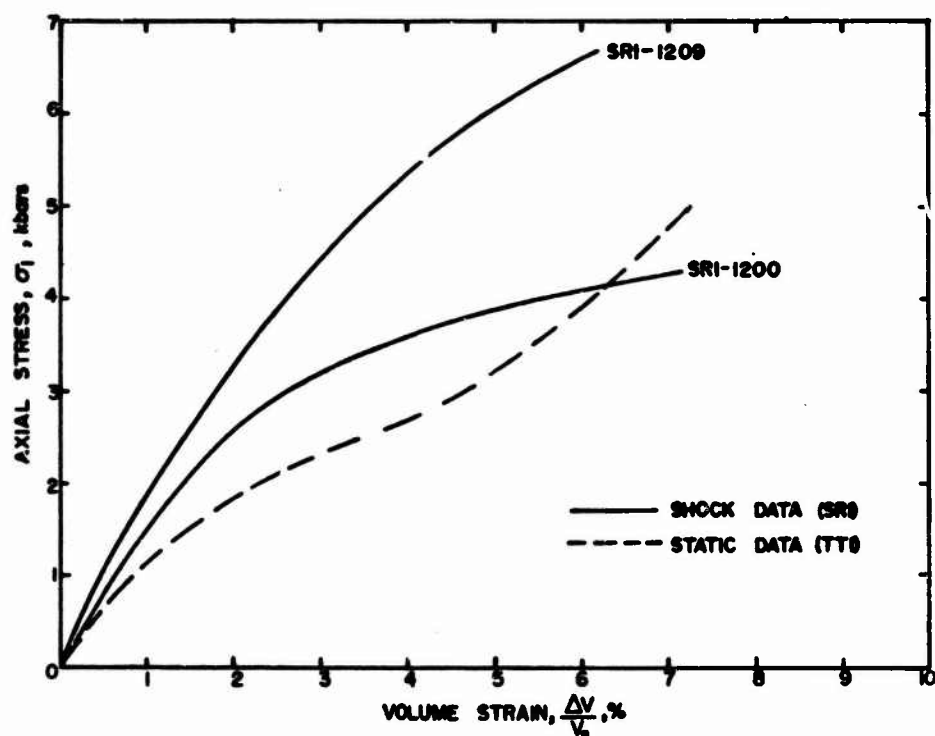
Figure 15.   Comparison of SRI plate-impact data
(reference 18) and static uniaxial strain
data on dry Mixed Company Sandstone.

IV. A THEORETICAL CONSTITUTIVE MODEL

Rocks generally possess a significant degree of porosity and, as has been shown in Sections II and III, exhibit pore collapse under hydrostatic pressure (a few tenths of a kilobar here). This behavior is in some ways similar to that of porous ductile metals subject to hydrostatic loading.[20-22] However, in ductile metals, an increase in mean normal stress results in pore compaction regardless of the deviatoric contribution, while rocks can undergo volume expansion in certain circumstances for which the mean stress is increasing. These effects of volume compaction and volume dilation have been mathematically described with reasonable success for a number of geological materials by the so-called 'cap model."[23-26] These models are all quite sophisticated and generally change in form depending on the material that is being described.

The important question that needs to be answered is what is the simplest model that can be used to represent the main features of rock behavior? To attempt to answer this question and, at the same time, obtain constitutive relations for the two materials investigated here, a special case of the cap model described by Green and Swanson for concrete[26] is used.

This model can be defined in terms of a pair of yield surfaces, which are most conveniently represented in terms of J_1 and J_2, the first and second invariants of the stress tensor:

$$J_1 = \sigma_{11} + \sigma_{22} + \sigma_{33}, \tag{1}$$

$$J_2 = \frac{1}{6}\left[(\sigma_{11} - \sigma_{22})^2 + (\sigma_{22} - \sigma_{33})^2 + (\sigma_{33} - \sigma_{11})^2\right]$$
$$+ \sigma_{12}^2 + \sigma_{23}^2 + \sigma_{31}^2. \tag{2}$$

Figure 16 shows the relative positions of the two yield surfaces in the J_1, $\sqrt{J_2}$ plane before (solid lines) and after (dashed lines) a triaxial compression test ACD. These surfaces are defined in terms of the functions F_1 and F_2 according to

$$F_1 (J_1, \sqrt{J_2}) - K_1 = 0, \tag{3}$$

$$F_2 (J_1, \sqrt{J_2}) - K_2 = 0, \tag{4}$$

where K_1 and K_2 are coefficients that increase with the amount of plastic flow and hardening that has taken place. The initial values of K_1 and K_2 are $\hat{K}_1$ and $\hat{K}_2$, respectively. The surface $F_1 - K_1 = 0$ determines the onset of plastic shear deformation, and, for the case of positive slope as shown in Figure 16, is the source of volume
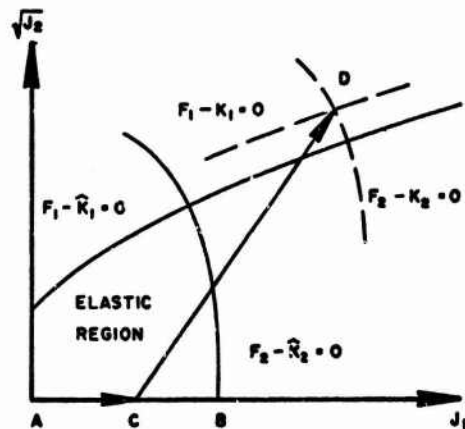

Figure 16.   Initial yield surface
             positions for cap model.

27

dilatancy when an associated flow rule is used to define the plastic strain components. Also, $F_2 - K_2 = 0$ defines the cap, which is necessary to account for volume compaction. For example, irreversible volume compaction occurs in hydrostatic compression when point B on the J_1 axis in Figure 16 is reached.

Because the yield surface consists of two independent segments, the plastic strain components, as determined by an associated flow rule, are given by Green and Swanson[26]

$$de_{ij}^p = \lambda_1 \frac{\partial F_1}{\partial \sigma_{ij}} + \lambda_2 \frac{\partial F_2}{\partial \sigma_{ij}},$$ (5)

where σ_{ij} is a component of the stress tensor and λ_1 and λ_2 are as yet undetermined multipliers. The total strain increment is given by the sum of de_{ij}^p and an elastic strain obtained from Hooke's law:

$$de_{ij} = de_{ij}^p + d\sigma_{ij}/2\mu - (1/6\mu - 1/9K)\, \delta_{ij}\, d J_1,$$ (6)

where K and μ are the bulk and shear moduli, and δ_{ij} is the Kronecker delta.

Each of the two yield surfaces is assumed to harden independently according to the following relationships:

$$dK_1 = (1/h_1)\, d\sqrt{I_2^p},$$ (7)

$$dK_2 = (1/h_2)\, de_{vc}^p,$$ (8)

where

$$d\sqrt{I_2^p} \equiv \left\{ \frac{1}{6} \left[(de_{11}^p - de_{22}^p)^2 + (de_{22}^p - de_{33}^p)^2 + (de_{33}^p - de_{11}^p)^2 \right] \right.$$
$$\left. + (de_{12}^p)^2 + (de_{13}^p)^2 + (de_{23}^p)^2 \right\}^{\frac{1}{2}}.$$ (9)

The term $d\epsilon_{vc}^p$ in Eq. (8) is the plastic volume compaction obtained from the surface $F_2 - K_2 = 0$. That is,

$$d\epsilon_{vc}^p = 3\lambda_2 \frac{\partial F_2}{\partial J_1} . \tag{10}$$

The terms h_1 and h_2 in Eqs. (7) and (8) can be functions of stress, plastic strain, etc. In fact, it is through the functions h_1 and h_2 that the details of the experimental data are fit by the theory.

It can be shown with considerable algebraic manipulation that, in the region of plastic deformation, λ_1 and λ_2 are given by[26]

$$\lambda_1 = \left[2h_1 \, dF_1 - \frac{\partial F_2}{\partial \sqrt{J_2}} \lambda_2 \right] \bigg/ \frac{\partial F_1}{\partial \sqrt{J_2}} , \tag{11}$$

$$\lambda_2 = h_2 \, dF_2 \bigg/ 3 \frac{\partial F_2}{\partial J_1} . \tag{12}$$

Equation (11) holds for $F_1 - K_1 = 0$ and $dF_1 > 0$, i.e., when the stress state is on the yield surface and in a condition of loading. Otherwise, λ_1 is equal to zero. Similar arguments apply to λ_2 and Eq. (12).

The functions F_1 and F_2 must be chosen in such a way as to represent the essential features of the experimental data without unnecessary complication in the analysis. This means that we do not want to choose functions that possess a great deal of sophistication unless it is found necessary in representing some important aspect of the data that cannot be described by simpler means. For this reason we choose the least complicated forms for F_1 and F_2 that will allow both volume dilatancy and significant volume compaction:

$$F_1 = \sqrt{J_2} - \alpha J_1, \tag{13}$$

$$F_2 = J_1. \tag{14}$$

Equation (13) defines a shear yielding surface of the Coulomb-Mohr type where α is the friction angle and Eq. (14) defines a vertical cap. It will be seen that these very simple functions go a long way in representing the mechanical properties of the dry tuff (NTS) and Mixed Company sandstone described in this report.

In order to represent the mechanical properties of a particular material, all that remains to be done is to specify the elastic moduli and the functions h_1 and h_2 in Eqs. (7) and (8). This is not generally an easy task and the functional form of h_1 and h_2 can change from one material to another. However, there are a few guidelines that can be followed in choosing these functions.

It is advantageous to deal with the deviatoric and hydrostatic effects separately: Eq. (7) is related to the deviatoric response and Eq. (8) determines the hydrostatic compaction properties. The plastic deviatoric strain increment is proportional to $d\sqrt{I_2^p}$ in Eq. (7), which can be written as

$$d\sqrt{I_2^p} = h_1 \, dF_1 = h_1(d\sqrt{J_2} - \alpha \, d J_1), \tag{15}$$

where Eq. (13) for the shear failure envelope has been used. From triaxial tests on rocks, it is generally found that the plastic strain increment for a given deviatoric stress increment increases with plastic strain and decreases with confining pressure; c.f., Figures 12a and 12b. Thus, these general effects must be reflected in a choice of the function h_1.

The amount of irreversible volume change due to pore compaction is controlled by Eq. (8) which can be written as

$$d\epsilon_{vc}^p = h_2 \, dF_2 = h_2 \, d J_1, \tag{16}$$

where Eq. (14) for the vertical cap has been used. The function h_2 is chosen to be large where the rate of plastic volume compaction is large, and *vice versa*. For example, when the material state approaches zero porosity in compaction, h_2 must vanish. From observation of mean normal stress and volume strain in triaxial tests, it is observed that the presence of deviatoric effects initially enhances the rate of plastic volume strain. All of these phenomena influence the choice of the function h_2.

To obtain a fit to the data on dry tuff (NTS) and Mixed Company sandstone presented in this report, the procedure outlined in the previous two paragraphs is followed. The actual choice of the functions h_1 and h_2, and the numerical values which go into the functions, is made by trial and error. This is precisely the approach that was used in developing a constitutive model for concrete.[26] One can start with simplified functional forms for h_1 and h_2 based on few adjustable parameters and it very soon becomes apparent that these simple expressions are not adequate for fitting all of the data. Consequently, the functional expressions become modified to a considerable extent and take on a fairly complex appearance. For the data presented here, the following functional forms for h_1 and h_2 were used with independent variables J_1, $\sqrt{J_2}$, K_1, etc. in units of kbar:

Tuff

$$h_1(\text{kbar}^{-1}) = \frac{0.056}{1 + 0.02\ J_1^2}\ \exp\left[1.62\ K_1/(1 + 0.038\ J_1)\right], \qquad (17)$$

$$h_2(\text{kbar}^{-1}) = 0.0043\left\{J_1\exp(-\ 0.075\ J_1^{1.4})\right.$$
$$\left. +\ \frac{4.31\left[1 - \exp(-\ 10\sqrt{J_2})\right]}{1 + 0.038\ J_1}\right\}\left(1 - \frac{\epsilon_{vc}^p}{0.30}\right)^{0.3}, \qquad (18)$$

$K = 200 - 164\ \exp(-\ 0.071\ J_1)$ kbar,

$\mu = 52$ kbar,

$\hat{K}_1 = 0,\ \hat{K}_2 = 1$ kbar,

$\alpha = 0.064.$

Sandstone

$$h_1(\text{kbar}^{-1}) = \frac{0.092}{1 + 0.1\ J_1^2}\ \exp(2\ K_1), \qquad (19)$$

$$h_2(\text{kbar}^{-1}) = 0.01\left\{f(J_1)\right.$$
$$\left. +\ 2.75\left[1 - \exp(-\sqrt{J_2})\right]\exp\left[-2.5\ f(J_1)\right]\right\}\left(1 - \frac{\epsilon_v^p}{0.21}\right)^{0.3}, \qquad (20)$$

$f(J_1) = 0,\ J_1 < 10.5$ kbar,

$f(J_1) = 1 - \exp\left[(10.5 - J_1)/3\right],\ J_1 \geq 10.5$ kbar,

$K = 130 - 120\ \exp(-\ J_1/3)$ kbar,

$\mu = 20$ kbar,

$\hat{K}_1 = \hat{K}_2 = 0,$

$\alpha = 0.082.$

Based on Eqs. (17) and (18), and numerical integration of Eqs. (5), (6), (11) and (12), calculations of the mechanical response of tuff under hydrostatic and triaxial testing conditions are shown in comparison with experimental data in Figures 17 and 18. A minor shortcoming to the model for shear deformation of dry tuff is the fact that it predicts a sharp yield point for the onset of plastic flow and the data (shown in Figure 17) do not indicate this behavior. The necessary modifications to the constitutive model in order to include the observed shear behavior are extensive and would require completely different hardening rules. However, it can be seen from these figures that the simple model based on the linear Coulomb-Mohr shear failure envelope and the vertical cap does a fairly good job in representing all the experimental data including the phenomenon of volume dilatancy as shown in Figure 18.

Similar calculations were compared with experimental data on Mixed Company sandstone and the results are shown in Figures 19 and 20. Again, all of the essential features of the experimental data have been represented.

In both cases it is believed that whatever discrepancies exist between theory and experiment are due to shortcomings in the functions h_1 and h_2 rather than to the choice of yield envelopes. For example, a reduction in α at large mean normal stress would result in greater disagreement between theory and experiments in Figures 18 and 20. Because of the rather cumbersome functions necessary to fit the data, it seems that we have not been judicious in the choice of the particular forms. This problem can be solved only by additional investigation of other functions in representing the mechanical behavior of

rocks. Nevertheless, the mathematical analysis presented here seems
to be as adequate as any work to date in describing the loading pro-
perties of rocks within the limits of experimental observation.

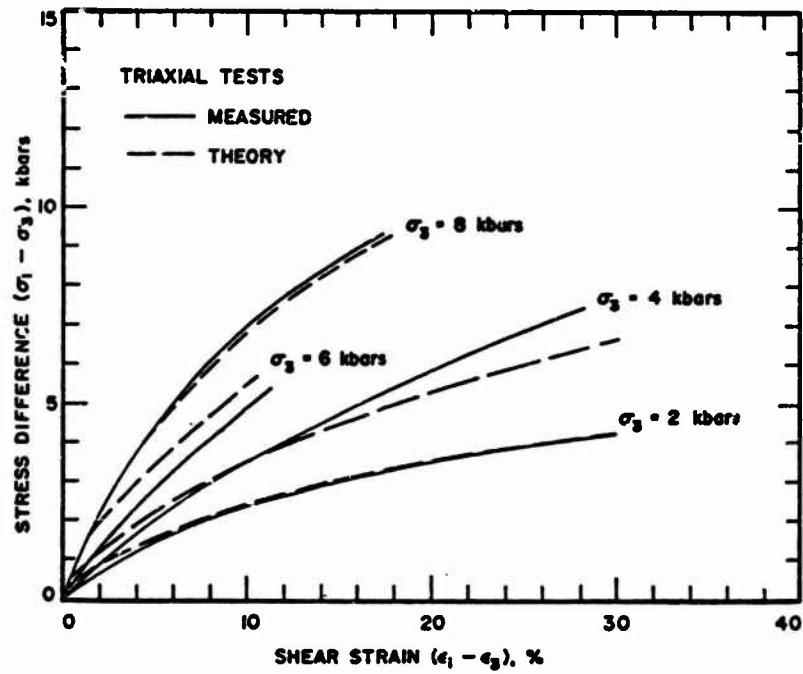Figure 17. Comparison of predicted and measured shear-
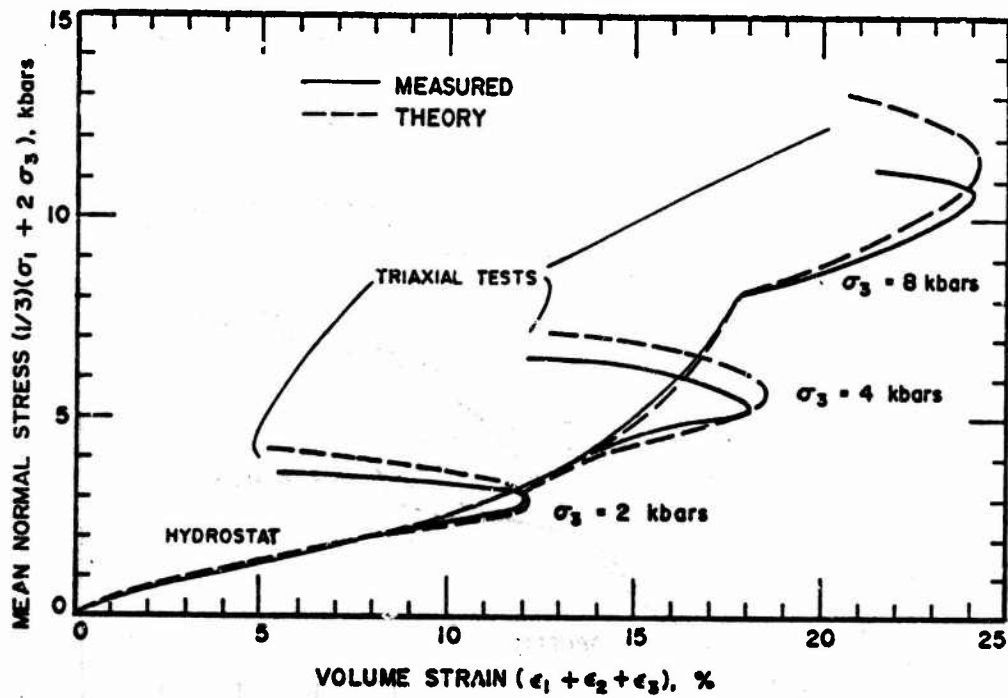strain response for dry NTS ash-fall tuff.

Figure 18. Comparison of predicted and measured volume-strain
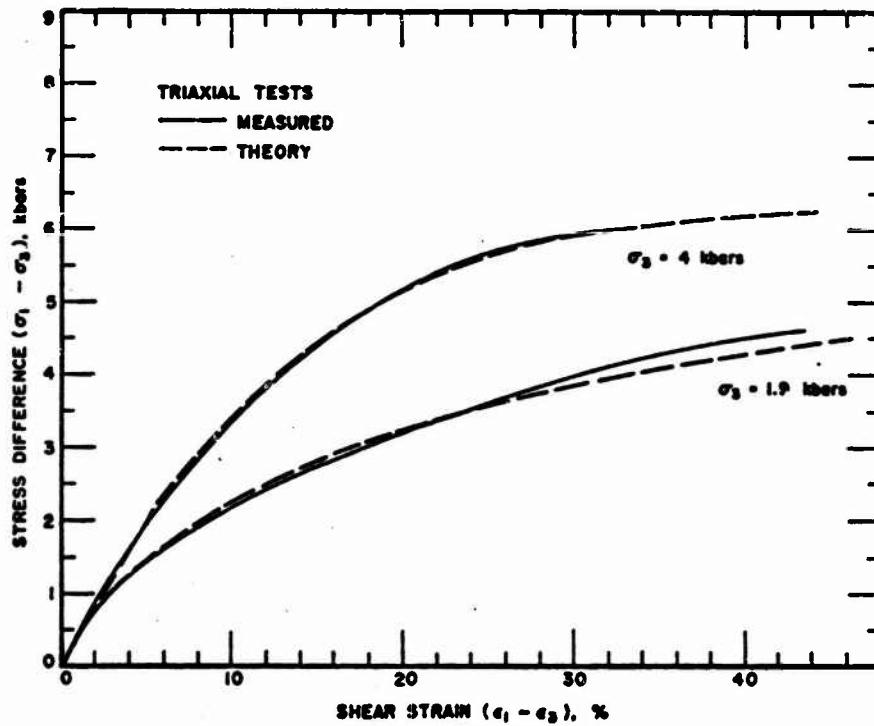response for dry NTS ash-fall tuff.

35

Figure 19. Comparison of predicted and measured shear-strain response for dry Mixed Company sandstone.
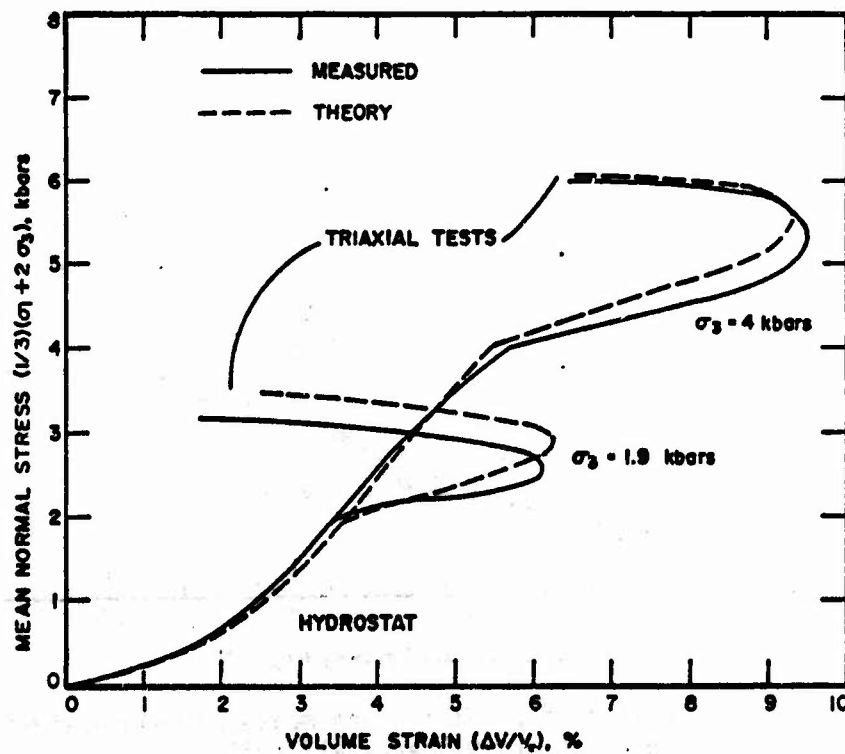

Figure 20. Comparison of predicted and measured volume-strain response for dry Mixed Company sandstone.

V. DISCUSSION AND CONCLUSIONS

The stress-strain measurements obtained show that two very
porous geologic materials--a dry tuff and a dry sandstone--exhibit
complex deformation and strength features. These are:

a. an increase in shear strength with mean normal stress,

b. large permanent compaction dependent upon both mean normal
    stress and shear stress,

c. path-dependent strains,

d. strong strain strengthening (work hardening),

e. volume compaction is followed by volume dilatancy for loading
    paths in which the ratio $d(\sigma_1 - \sigma_3)/d(\sigma_3)$ is sufficiently
    large (such as the uniaxial compression test performed here).

The general features above are exhibited by both rocks. However,
observation of the micro-structure of each material showed some dif-
ferences. The tuff contains pores from Angstrom size (10^{-7} mm) to
millimeter size, with much of the porosity believed to be 10^{-2} mm and
below.[27] Apparently relatively little of the total porosity exists
as open microcracks. The sandstone, contains most of its porosity
in the form of holes about 0.1 mm, plus some amount of fracture
(microcrack) porosity.

Elasticity, even non-linear elasticity, cannot fit the observed
general features, nor can simple plasticity handle both the compaction
and the dilation observed. The only theory that can presently accom-
modate all the above features is the "cap model." This model has been
fit to the observed stress-strain response using a relatively simple
hardening law, Eqs. (7) and (8). The model handles the crushup under hy-
drostatic pressure, enhanced compaction under various shear stress,

37

volume dilation under some load paths, work hardening and the effect of mean normal stress on shear strength. For the hydrostatic pressure and triaxial-stress load paths presented here, the model fits the stress-strain response relatively well. To compare experiment and theory for uniaxial strain requires a different calculation than presented in this report. However, it is expected that the model presented here should give reasonable agreement with the measured uniaxial-strain response.

The most difficult features to model--regions that currently need more research--are (i) the tensile and very low mean normal stress region and (ii) the hardening that occurs for various load paths. A combination of theoretical modeling and experiments are needed to extend the cap model to adequately cover these two regions.

Additionally, to model in-situ rock masses many real-world in-situ features must be considered. Such real effects as anisotropy (tectonic-stress induced and natural) and nonhomogeneity, joints and faults, in-situ stress and moisture content and pore pressure must be considered. Modeling these features was not the intent of this work; some of the effects can be addressed in the laboratory, while others will require field work experimentation.

IV. REFERENCES

1. W. S. Brown and S. R. Swanson, "Constitutive Equations for Westerly Granite and Cedar City Tonalite for Variety of Loading Conditions," Report 2473, Defense Atomic Support Agency, March 1970.

2a. S. J. Green, R. M. Griffin and H. R. Pratt, "Stress-Strain and Failure Properties of Porous Shale," Terra Tek report TR 71-12 and Proceedings Sixth Conference on Drilling and Rock Mechanics, Austin, Texas, January 1973.

2b. S. J. Green, R. M. Griffin, A. D. Black, S. W. Butters, S. W. Duncan, H. R. Pratt and K. B. Watson, "High Pressure Properties of Several Nevada Test Site Tuffs," Defense Nuclear Agency Final Report DNA 2814F under Contract DASA01-71-C-0079, August 1971.

2c. S. J. Green, S. W. Butters and R. M. Griffin, "High Pressure Properties of U12n.05 and U12t.02 Tuffs, Nevada Test Site," Defense Nuclear Agency Final Report DNA 3055F under Contract DNA001-72-C-0006, April 1973.

2d. S. J. Green and S. W. Butters, "Material Properties for Mine Dust High Explosive Test (Stemming Mechanics Study Three)," Terra Tek Report TR 72-15 prepared for Defense Nuclear Agency, September 1972.

2e. S. W. Butters, R. J. Reid, S. J. Green and A. H. Jones, "Mechanical Properties of Nevada Test Site Tuffs from Selected Exploratory Drill Holes," Defense Nuclear Agency Final Report DNA 3181F under Contract DNA001-73-C-0017, September 1973.

3. J. LaComb, Defense Nuclear Agency, Nevada Test Site, Mercury, Nevada, all test specimens were provided by Defense Nuclear Agency.

4. All test specimens were received from the Department of Defense Mixed Company High-Energy Explosive test site. The cores were taken by the U.S. Army Waterways Experiment Station and shipped to Terra Tek by Defense Nuclear Agency.

5. S. R. Swanson and W. S. Brown, "An Observation of Loading Path Independence of Fracture in Rock," *Int. J. Rock Mech. Min. Sci.*, *8*, pp. 277-281, 1971.

6. S. W. Butters, R. J. Reid, R. Lingle, A. H. Jones and S. J. Green, "Material Properties for Husky Ace Containment Evaluation," Terra Tek Report TR 73-41, August 1973.

7.   R. Lingle, Ultrasonic Measurements were made at Terra Tek, Inc.
            using techniques as previously used for porous rocks,
            1973.

8.   R. D. Perkins, A. H. Jones, S. J. Green and J. D. Leasia, "Deter-
            mination of Multiaxial Stress Behavior of Solenhofen
            Limestone and Westerly Granite," Defense Atomic
            Support Agency Final Report DASA-2438 under Contract
            DASA-01-69-C-0104, December 1970.

9.   D. R. Stevens, H. C. Heard and R. N. Schock, "High Pressure
            Mechanical Properties of Tuff from the Diamond Mine
            Site," Lawrence Livermore Laboratory Report UCRL-
            50858, 1970 and H. C. Heard, R. N. Schock, D. R.
            Stevens, "High Pressure Mechanical Properties of Tuff
            from the Diamond Mine Site," Lawrence Livermore
            Laboratory, UCRL-51099, 1971.

10.   A. H. Jones and S. J. Green, "The Role of Material Properties in
            Determining Ground Motion from High Energy Detonations,"
            Defense Nuclear Agency Final Report DNA 3056F under
            Contract DNA001-72-C-0006, April 1973.

11.   W. F. Brace, B. W. Paulding and C. Scholz, "Dilatancy in the
            Fracture of Crystalline Rocks, *J. Geophys. Res., 71,*
            p. 3939, 1966.

12.   W. F. Brace, "Micromechanics in Rock Systems," in *Structure,*
            Solid Mechanics and Engineering Design, edited by
            M. Te'eni (John Wiley and Sons Ltd, London, 1971)
            p. 187.

13.   J. Handin, "Strength and Ductility," in *Handbook of Physical*
            Constants, edited by S. P. Clark, Jr. (The Geological
            Society of America, New York, 1966) p. 223.

14.   E. C. Robertson, "Experimental Study of the Strength of Rocks,"
            Bull, Geol. Soc. Am., 66, p. 1275, 1955, and H. C.
            Heard, "Transition from Brittle to Ductile Flow in
            Solenhofen Limestone as a Function of Temperature,
            Confining Pressure and Interstitial Fluid Pressure,
            Rock Deformation, Geo. Soc. of Am., Memoir 79, p. 193,
            1960.

15.   W. R. Wawersik, "Detailed Analysis of Rock Failure in Laboratory
            Compression Tests," Thesis, University of Minnesota,
            July 1968.

16.   S. J. Green and S. W. Butters, unpublished test results, tests
            at Terra Tek, Inc. 1973.

17. S. R. Swanson, "Representation of the Post-fracture Mechanical Behavior of Nugget Sandstone," Defense Nuclear Agency Final Report DASA 2721 under Contract DASA 01-70-C-0072, 1971.

18. C. F. Peterson and D. C. Erlich, "Dynamic Properties of Rock Required for Prediction Calculations," Defense Nuclear Agency Final Report DNA-3123 under Contract DASA01-71-C-0094, November 1972.

19. A. H. Jones, R. J. Christensen and S. J. Green, "Effect of Strain Rate Loading on Porous, Partially Saturated and Dry Rock," Terra Tek Report TR 73-21, September 1973.

20. B. M. Butcher and C. H. Karnes, "Dynamic Compaction of Porous Iron," *J. Appl. Phys., 40,* p. 2967, 1969.

21. R. R. Boade, "Compression of Porous Copper by Shock Waves," *J. Appl. Phys., 39,* p. 5693, 1968.

22. W. Herrmann, "Constitutive Equation for Ductile Porous Materials," *J. Appl. Phys., 40,* p. 2490, 1969.

23. I. Nelson, M. L. Baron and I. Sandler, "Mathematical Models for Geological Materials for Wave Propagation Studies," in *Shock Waves and Mechanical Properties of Solids,* edited by J. J. Burke and V. Weiss (Syracuse University Press, Syracuse, N. Y., 1971) p. 289.

24. S. R. Swanson, "Development of Constitutive Equations for Rock," Ph.D. Thesis, University of Utah, Salt Lake City, Utah, 1969.

25. T. D. Riney, et al., "Ground Motion Models and Computer Techniques," Systems, Science and Software Report 3SR-1071, April 1972.

26. S. J. Green and S. R. Swanson, "Static Constitutive Relations for Concrete," Terra Tek, Inc. Report TR 71-34, December 1972.

27. H. S. Swolfs, H. R. Pratt, S. J. Green and A. H. Jones, "Preliminary Observations of the Microstructure of Nevada Test Site Tuffs," Terra Tek Report TR 73-32, July 1973.

28. W. F. Brace, "Effect of Pressure on Electrical Resistance Strain Gages," *Experimental Mechanics, 4,* pp. 212-216, 1964.

29. R. N. Schock and A. G. Duba, "Pressure Effect on the Response of Foil Strain Gages," *Experimental Mechanics, 13,* pp. 43-44, 1973.

ACKNOWLEDGMENTS

42

APPENDIX A

DETAILED EXPERIMENTAL TECHNIQUES

Stress and Strain Measuring Devices

Figure A-1 is a photograph of a test assembly showing stress and strain sensors employed in a typical test. An important feature of the testing system described below is that all principal stress and strain components of the specimen are measured. Measurements are performed in a high hydrostatic pressure environment. Hydrostatic pressure, σ_3, is monitored by a 350 ohm manganin wire coil connected electrically as a single active leg of a Wheatstone bridge. Stress-difference, $(\sigma_1 - \sigma_3)$, is monitored by a strain-gaged load cell of conventional design in the form of a high-strength steel cylinder. Calibration of these transducers is performed using precision laboratory standards for pressure (a 7 kbar Heise gage) and force (a 6400 kilobram proving ring).

The strain transducers measure the axial strain, ε_1, and transverse strain, $\varepsilon_2 = \varepsilon_3$. The axial strain transducer which can monitor a 30% axial shortening strain (reference length is 3.81 cm) with an accuracy of 0.16% strain, is shown in Figure A-2. There are four thin cantilevered-beam arms which are strain-gaged (350 ohms) on both flat sides and wired into a four-legged Wheatstone bridge with two active gages in each leg. These four arms are rigidly attached to the base ring which is mounted to the hardened steel specimen lower endcap. When displacement occurs in the specimen, the displacement ring mounted to the upper endcap displaces the cantilever arm tips along a conically tapered surface. The resulting strain-gage bridge unbalance is self-compensating for the small rotations of the endcaps sometimes
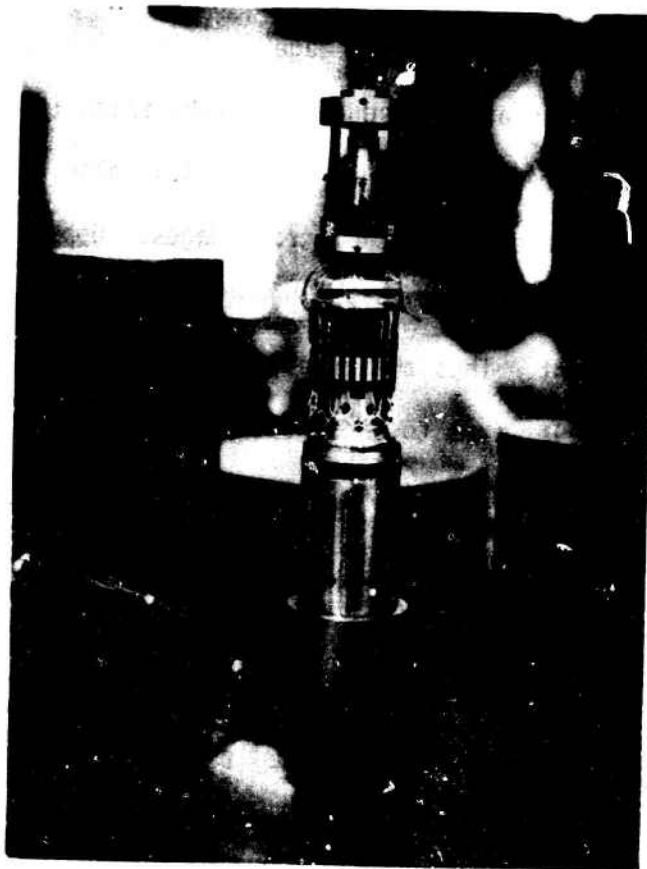
44

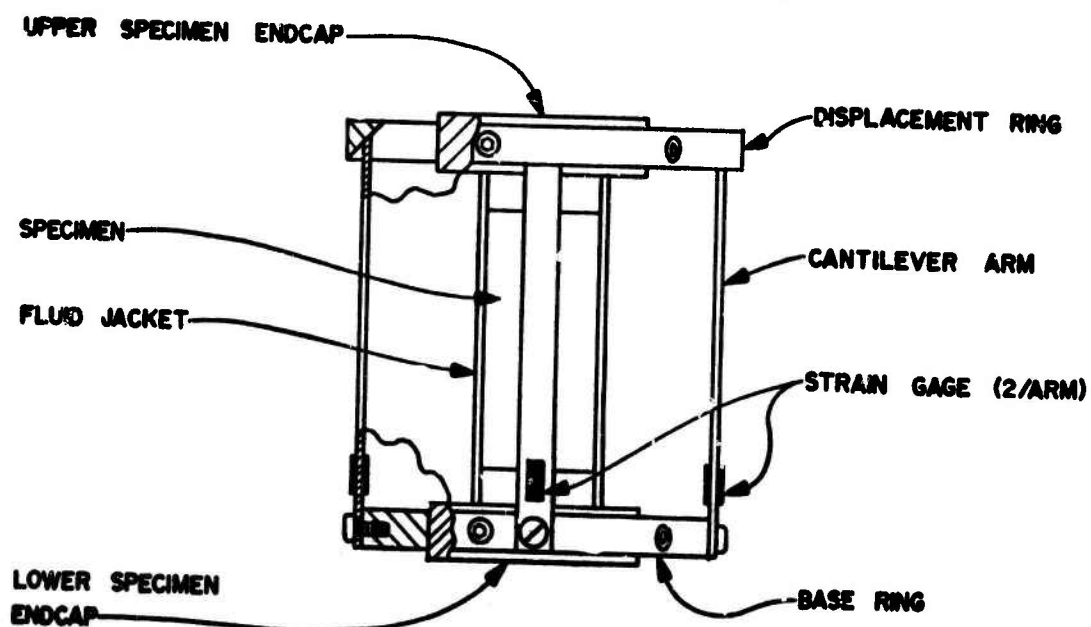Figure A-1. Specimen transducer assembly.

Figure A-2. Schematic of axial strain transducer.

45

encountered while hydrostatically loading a specimen. Calibration over the entire strain measurement range of the transducer is performed using a laboratory precision height gage.

The transverse strain transducers (establishing the orthogonal axes for ϵ_2 and ϵ_3) are cantilevered-beam systems also. Two pairs of cantilevered arms each carry two strain-gages. Opposite arms are wired into a single Wheatstone bridge permitting measurement of diametric displacement. Thus the transducer relies upon the spring force of the cantilever arms to sense the specimen diameter. The contactor screws allow the arms to be pre-strained by an amount sufficient to maintain contact during a diametric strain of about 8% (for 19 mm reference diameter). Calibration of these cantilevers is performed in a manner similar to the axial transducer.

Two sets of strain transducers were developed, each for a specific test type. For hydrostatic pressure-volume and triaxial tests a set of axial and transverse cantilevers was used to track the large volume strain (up to approximately ±8% for each axis) with an accuracy of .10% strain.

A second set of transverse strain transducers was developed exclusively for static uniaxial-strain tests. The sensor illustrated in Figure A-3 was used to monitor and control diametric strains at
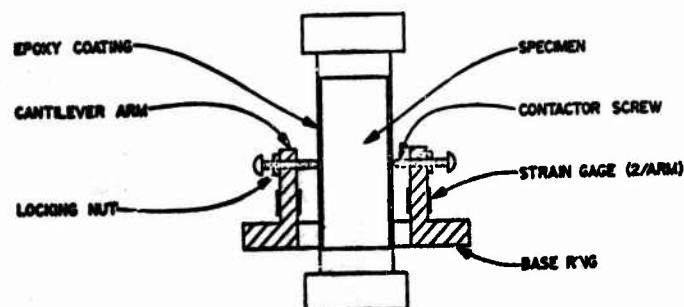

Figure A-3. Transverse strain cantilever system used for uniaxial-strain tests.

46

and near zero. This transducer has a strain range of ±1% of the 19 mm
reference diameter and can be used to maintain zero strain with an
accuracy of .005% (50 μstrains) for homogeneous materials. For large
porosity, non-homogeneous rocks, this high accuracy was not attained.
Aside from the non-uniformity of the distribution of pores and
granular materials in the rock, the sample surface plays an important
role. The urethane jacketing material is known to intrude into
openings with diameters of the order of .1 to .5 mm at high pressures.
This intrusion necessarily reduces the jacket thickness locally,
thereby causing uncertainty in the jacket effect on the pretest cali-
bration. Our best estimate of the measurement and control of zero
lateral strain is an accuracy of .05% strain.

Small-Strain Approximation

Throughout this work we have estimated the volume strain accord-
ing to the small-strain approximation: $\varepsilon_v = \sum_i \varepsilon_i$. The exact expres-
sion for volume strain includes second- and third-order terms in the
component strains. That is,

$$\Delta V/V_0 = \varepsilon_v + \sum_{ij} \varepsilon_i \varepsilon_j + \varepsilon_1 \varepsilon_2 \varepsilon_3. \tag{A-1}$$

Let us define the higher order terms in Eq. (A-1) as E, the error
involved in making the approximation $\Delta V/V_0 = \varepsilon_v$. Values of E/ε_v are
then given in Table A-1 for the maximum pressures achieved in hydro-
static tests and for maximum volume strains achieved in triaxial tests
presented in this report. The error (< 7%) introduced by this
approximation is within the experimental scatter caused by sample

47

TABLE A-1. ERROR INTRODUCED BY THE SMALL-STRAIN APPROXIMATION

Material	σ_1 (kbar)	σ_3 (kbar)	E/ε_v (%)
Tuff	8.0*	8.0*	7.0
"	5.0	2.0	2.5
"	7.8	4.0	4.2
"	16.3	8.0	7.0
Sandstone	8.0*	8.0*	5.0
"	3.7	1.9	1.0
"	8.5	4.0	5.0

* hydrostat

variability. However, larger errors result when the small strain
approximation is used in regions of high volume dilatancy. This has
negligible influence on the experimental and theoretical results
presented here.

Transducer Pressure Effects

When strain-gages are exposed to high pressures, a component
of the strain measurement is a pressure-induced apparent strain. This
pressure effect on single gages has been described in the literature.[28,29]
Tests have shown that the pressure-induced effects are independent of
high-pressure electrical feed-throughs, in-vessel lead connectors,
solder connections and external circuitry.[28] Also, apparent strain
due to pressure was found to be independent of pre-set strain condi-
tion. Tests performed in persuance of a solution to this problem
have shown that the repeatability of the apparent strain output for
a single gage in the high pressure environment depends on two para-
meters: (i) the thickness of the epoxy bonding layer and (ii) the rate
of pressure application. A method has been developed to reproducibly
attach strain-gages with a bonding thickness of ~3 μ. Tests are now

48

performed at the pressurization rate of about 1/4 kbar/minute for hydrostatic tests. Particular care is paid in placement of the strain gages.

Ten Kilobar Testing System

A block diagram of the 10 kbar system used for the tests described here is shown in Figure A-4. The two main press components are the loading system and the pressure intensifier system. Figure A-5 is a photograph of the loading frame showing the reaction platens, support columns, tie rods and hydraulic loading actuator. The test vessel is suspended from the upper platen by a split support-ring. A one-inch diameter loading-piston is attached to a 104,000 kg actuator and is guided by the loading-piston seal surface of the test vessel.
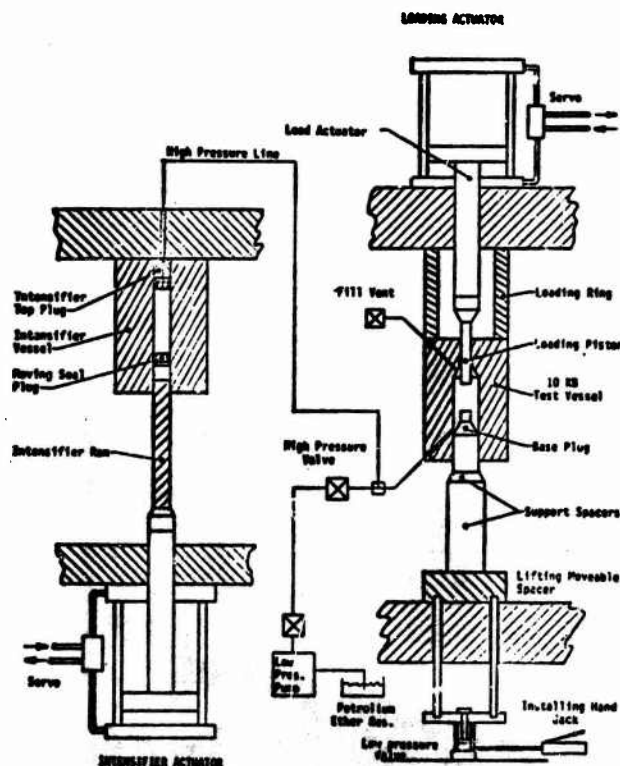
Figure A-4. Block diagram of 10 kbar testing machine.

A 5-cm diameter base plug supports the specimen, strain sensors, pressure coil, load cell and contains a Bridgman-type seal and 24 high-pressure conical electrical feedthroughs. Figure A-1 shows the base plug with specimen sensors mounted. The base plug also transmits the specimen axial loading thrust through its support spacers to the platens. A small hydraulic handjack is used to overcome the base plug seal friction and insert the base plug test assembly.

The pressure intensifier ram is attached to a 107,000 kg hydraulic actuator and with a single full stroke produces a pressure in excess of 11 kbars in the test system. The lower plug contains a moving high-pressure seal and rides freely on the intensifier ram. For ease
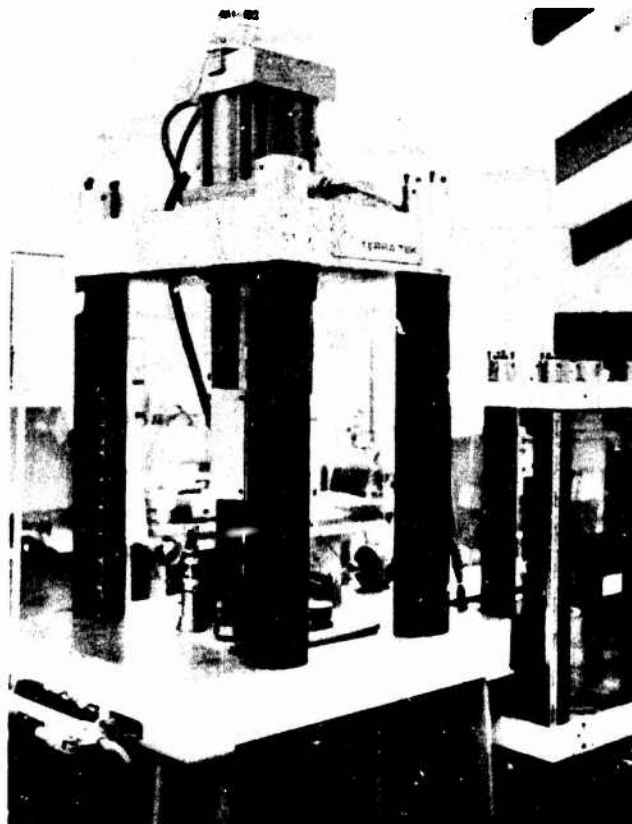

Figure A-5.   10 kbar system loading frame.

of operation a low pressure pump may also be used to pre-charge the system (up to about 0.7 kbars) as well as fill the test vessel. Both the test vessel and the pressure intensifier vessels are 4340 steel that have been autofretteged (strain strengthened) to a condition that prevents further yielding at 10 kbars internal pressure.

Servocontrolled System

Both press components are servocontrolled as illustrated in Figure A-6. The details of selected type of sensor feedback, command function, loading-stress-rate or strain-rate, etc., are determined by the type of test performed. Categories of tests include (a) hydrostatic, (b) uniaxial-strain, (c) confined triaxial-compression or other stress/strain histories.
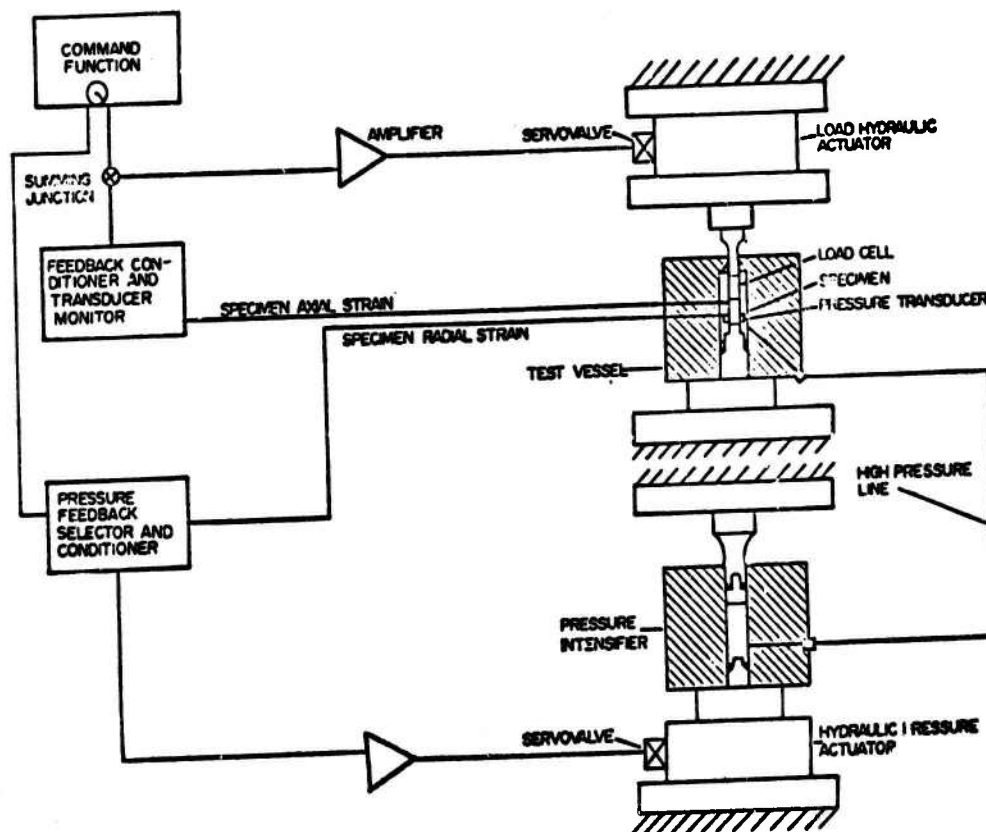

Figure A-6. Servocontrol system.

a. Hydrostatic tests are performed in which the three principal strains are recorded plus the fluid pressure (symmetrical stress loading). For these tests the command function generator produces a symmetrical sawtoothed voltage ramp (frequency less or equal to 0.001 Hz) for the intensifier servocontroller. The pressure feedback monitor conditions the servo output signal for a null offset. Strains and pressure data are recorded during the ramp cycle.

b. Uniaxial-strain tests are performed in the following manner: a pretest run (no test specimen within the vessel) to maximum pressure is performed while recording the pressure-effects of the transverse strain sensors on an analog chart recorder. The command function generator is set to provide the voltage ramp (frequency less or equal to 0.001 Hz) for either the intensifier or load controller. If the pressure servocontroller is selected, the load actuator is manually controlled and *vice versa*. As the pressure increases, load is applied to the specimen to just compensate for the pressure-induced compressive diametric strains. When zero transverse strain is achieved, the transverse strains sensors output follows exactly along the pretest tracing.

c. In triaxial-compression tests, a hydrostatic loading test is initially performed to the desired confining pressure. The command function generator is then set to provide voltage ramp (frequency less or equal to 0.001 Hz) for load. As load increases, the three principal strains, fluid pressure and the load (stress difference) are recorded.

52

Data Acquisition System

Figure A-7 shows the data acquisition system used for the tests described below. A Digital Equipment Corporation PDP Lab 11/20 computer is the primary recording device and provides real-time test data monitoring and analysis. Each test sensor provides input to one channel of an 8-channel, 12-bit, analog-to-digital converter which operates over a 10 volt range with a maximum resolution of 2.4 milli-volts (equivalent to 5 microvolts out-of-balance voltage at the bridge). The computer console contains the central processor, core memory, a two-color CRT plotting screen, a high-speed paper tape punch and reader and the A/D converter. Peripherals are addressable in real-time which allows instantaneous review of acquired data and test progress. Both the CRT plotter and the Valtech digital plotter are used to display post-test results.
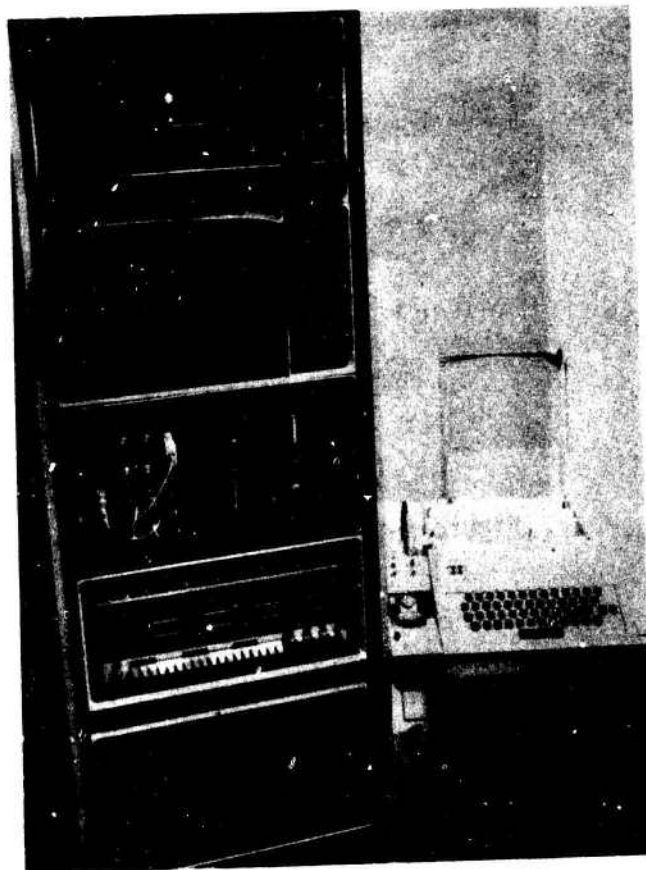

Figure A-7. Data acquisition system.

The instrumentation console shown in Figure A-8 contains
Wheatstone bridge current supplies, hookup patchboards, balancing
networks, calibration shunt networks and output amplifiers for
eight channels of data. Normally only five channels are used;
pressure, load, axial strain and two transverse strains. Data
monitoring using X-Y recorders as output terminals is also available
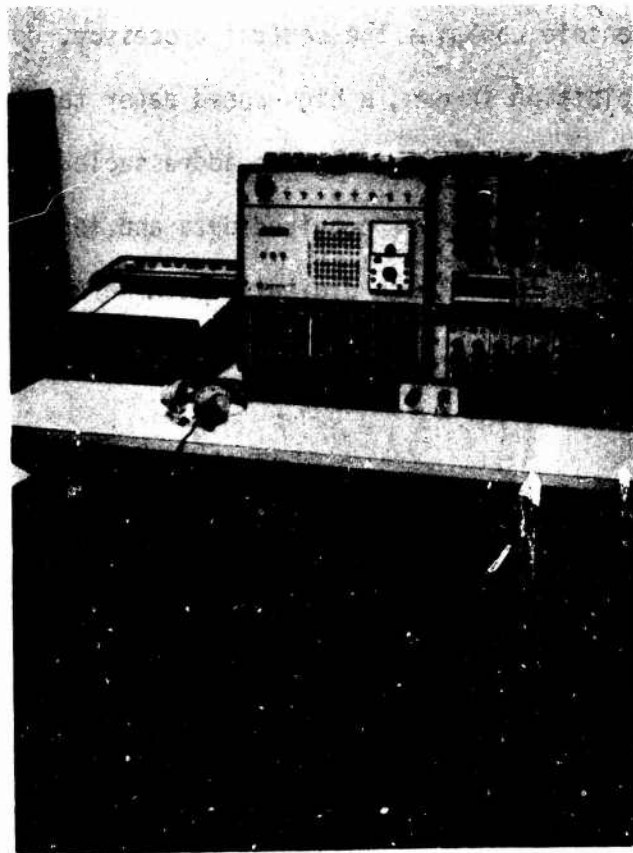at the testing machine servo-control console.

Figure A-8. Instrumentation console.

APPENDIX B

DETAILED MATERIAL DESCRIPTION AND SPECIMEN PREPARATION

The Nevada Test Site tuff samples were obtained from the left rib of tunnel U12e.06 between stations #9 +95 and #10 +50. This tunnel is located in the Rainier Mesa, Nevada Test Site, Mercury, Nevada, within ash-fall tuff, containing both reworked ash-fall and tuffaceous sandstone. The samples are mottled pink and are mainly fine grained with grains of less than 1 mm, but contain occasional coarser fragments of pumice granules, lithic grains and phenocrysts greater than 2 to 5 mm in size. Figure B-1 shows a photomicrograph at 50 times magnification. The glass shards that originally formed most of the matrix were crystallized as zeolites, cristobalite and possibly clay. Under standard room conditions, the density for the
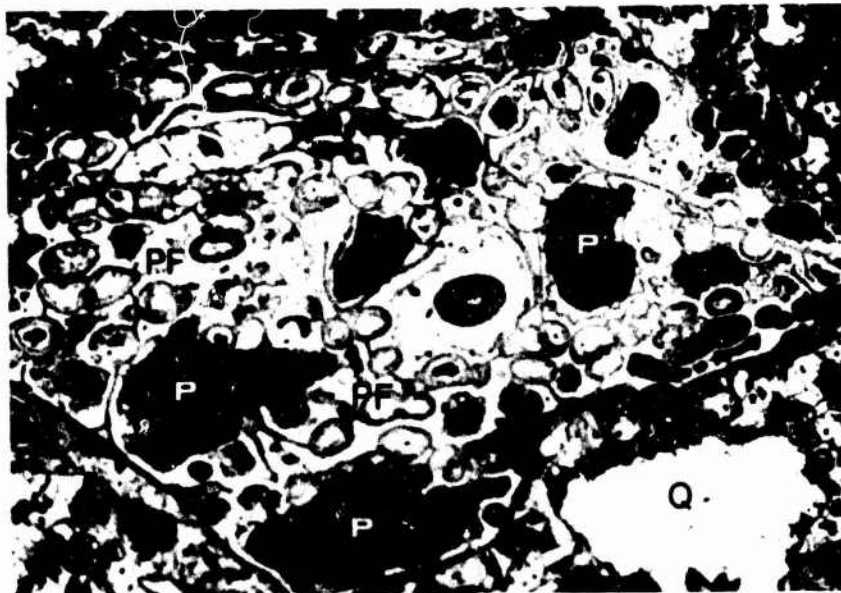
P-Pores
PF-Pumice Fragments
Q-Quartz

Figure B-1. Polarized reflected-light photomicrograph of ash-fall tuff showing intragranular porosity and microporosity inside pumice fragments.

samples is approximately 1.7 gm/cm^3 with grain density of approximately 2.46 gm/cm^3. Porosity, as derived from the relation

$$n = (1 - \rho_d/\rho_g) \times 100$$

where ρ_d, ρ_g are the dry and grain density respectively, is 31 percent.

The other porous rock tested in this program is from the Mixed Company test site near Grand Junction, Colorado. It is a massive, medium-grained, buff-colored sandstone. Microscopic examination indicates it is composed of almost 100% rounded quartz grains bonded with silica. Figure B-2 shows a photomicrograph at 50 times magnification. Grain size is 0.5 to 1.0 mm. Variations in density (1.94 to 2.03 gm/cc) can be attributed to variations in porosity rather than any difference in mineralogy. The rock is highly permeable and is

Figure B-2. Thin section photomicrograph of Mixed Company sandstone showing intragranular porosity and quartz grains. Q stands for quartz, R for rock fragment (microcrystalline), h for pores, F for feldspar.

friable when wet. Intact cores a few feet in length can be extracted indicating the rock's massive nature. However, faint relict bedding planes are observed on a macro-scale within the unit.

Test specimens were obtained from a 36-cm diameter drill hole in Area B (the Physics International Site) some 122 meters south, southeast of the working point of a 453.5 metric ton surface high explosive test. Typical dry laboratory density was 2.0 gm/cm^3; the corresponding grain density was 2.66 gm/cm^3 giving an average porosity of approximately 25%.

Specimens used for the tests were dry, solid, right-circular cylinders 1.9-cm diameter by 3.8-cm in length. A 1.9-cm core drill was used to core the specimens from larger blocks. The ends were ground with a precision surface grinder to be as smooth as the rock granularity allowed (~.003 cm rms) and parallel within ±.002 cm. The density of each specimen was determined by weighing the specimen (±.01 gm) and dividing by the calculated volume found by averaging measurements of the sample dimensions. Lengths and diameters were measured accurately to ±.003 cm. By this procedure the estimated density accuracy was ±.01 gm/cm^3.